

Magma storage and degassing beneath the youngest volcanoes of the Massif Central (France): lessons for the monitoring of a dormant volcanic province

G. Boudoire^{1,2*}, G. Padeloup¹, F. Schiavi¹, N. Cluzel¹, V. Rafflin¹, F. Grassa², G. Giuffrida³, M. Liuzzo^{2,4}, A. Harris¹, D. Laporte¹, A.L. Rizzo^{2,5}

¹UCA, CNRS, IRD, OPGC, Laboratoire Magmas et Volcans, 6 avenue Blaise Pascal, 63178 Aubière, France

²Istituto Nazionale di Geofisica e Vulcanologia, Sezione di Palermo, Palermo, Italy

³Istituto Nazionale di Geofisica e Vulcanologia, Sezione di Catania, Catania, Italy

⁴Dipartimento di Fisica e Scienze della Terra, Università di Ferrara, Ferrara, Italy

⁵Istituto Nazionale di Geofisica e Vulcanologia, Sezione di Milano, Milano, Italy

* Corresponding author. Present address : Laboratoire Magmas et Volcans, Campus universitaire des Cézeaux, 6 Avenue Blaise Pascal, 63170 Aubière, France. Telephone: +33 (0)4 73 34 67 23. E-mail: guillaume.boudoire@uca.fr.

Abstract

Developing appropriate monitoring strategies in long-quiescent volcanic provinces is challenging due to the rarity of recordable geochemical and geophysical signals and the lack of experienced eruptive phenomenology in living memory. It is the case in the Massif Central (France) where the last eruptive sequence formed the Pavin's Group of Volcanoes, about 7 ka ago. There, current evidence of a mantle activity reminiscence is suggested by the presence of hydrothermal springwaters, mofettes, and soil degassing. It appears fundamental as a prerequisite to decipher the evolution of the gas phase in the magmatic system at the time of the eruptive activity to understand the meaning of current local gas emissions. In this study, we develop an innovative approach coupling CO₂ densimetry and geochemistry of fluid inclusions from products erupted by the Pavin's Group of Volcanoes. 3D imagery by Raman spectroscopy revealed that carbonate forming in fluid inclusions may lead to underestimate CO₂ density in fluid inclusions by up to 50 % and thus to unreliable barometric estimates. Fortunately, we found that this effect may be limited by focusing on fluid inclusions with a small diameter (<4 µm) and where no solid phase is detected on Raman spectra. The time evolution of the eruptions of the Pavin's Group of Volcanoes shows a progressive decrease of the depth of magma storage (from more than 9 kbar down to 1.5-2 kbar) in parallel to magma differentiation (from basanites at Montcineyre to benmoreites at Pavin). The geochemical analysis of the noble gases entrapped in fluid inclusions yielded two main conclusions: (1) ³He/⁴He ratio (6.5-6.8 Ra) is in the range of ratios measured in fluid inclusions from mantle xenoliths in the Massif Central (5.6±1.1 Ra, on average) suggesting partial melting of the subcontinental lithospheric mantle, and (2) magma degassing (⁴He/⁴⁰Ar* from 4.0 to 16.2) mirrors magma differentiation and the progressive rise of the magma ponding zones of the Pavin's Group of Volcanoes. According to our modelling, about 80 % of the initial gas phase would be already exsolved from these magmas, even if stored at mantle depth. Based on the results obtained from fluid inclusions, we propose a model of the evolution of the signature of noble gases and carbon isotopes from mantle depth to crustal levels. In this frame, gas emissions currently emitted in the area (Rc/Ra = 6.1-6.7 and ⁴He/⁴⁰Ar* = 1.7) point to an origin in the lithospheric mantle. This study strongly encourages the establishment of a regular sampling of local gas emissions to detect potential geochemical variations that may reflect a change from current steady-state conditions.

Keywords

Fluid inclusions, Barometry, Noble gases, Magma degassing, Monitoring

1. Introduction

The global population growth raises severe issues about our way to live in a sustainable world and to face natural disasters. With almost one in eight people living within 100 kilometres of an active volcano (Brown et al., 2015), volcanic eruptions constitute one of the main natural hazards for the

humanity (Oppenheimer, 2015). In this regard, long-quiet volcanic provinces play a peculiar role. On the one hand, the almost no trace of eruptive activity in the collective memory tends to favour the settling of local populations and socio-economic development on lands covered by fertile volcanic soils (Shoji and Takahashi, 2002). It is even truer in Southern countries where agriculture represents often one of the main economic sources and is fundamental for the survival of local populations. On the other hand, long periods of quiescence may strongly favour the energy accumulation at depth and drive magmas near a critical pressure point leading to violent eruptions (Chiodini et al., 2016). This parallel evolution significantly increases the probability of fatal eruptions, even more considering the lack of preparedness of local population in face of a natural hazard with a low occurrence frequency. The development of appropriate monitoring strategies in long-quiet volcanic provinces is also challenged by (1) the rarity of signals that may indicate residual magmatic activity, and (2) the difficulty of convincing decision-makers of the necessity to implement a policy of prevention (rather than reaction) in face of an a priori non-imminent risk. It is the case of the French Massif Central (France), where the last known eruption is dated at $6,730 \pm 170$ BP (Juvigné and Mialler, 2016). The presence of surface manifestations of a potential 'residual' magmatic activity is testified by the numerous hydrothermal springs spread over the territory with clear magmatic origin (Matthews et al., 1987; Bräuer et al., 2017; Moreira et al., 2018), together with areas of intense soil (CO_2 -Rn) degassing (Battani et al., 2010; Gal and Gadalia, 2011; Gal et al., 2018). However, both types of occurrences remain poorly documented to date. Although fundamental to the development of regional monitoring strategies, there is no consensus on the origin of the degassing. Some studies suggest the presence of still partially molten mid-crustal reservoirs beneath the area (Martel et al., 2013; France et al., 2016), while others refer to fluid transport in deep reaching faults from magmatic reservoirs within the subcontinental lithospheric mantle (SCLM; Bräuer et al., 2017).

Previous studies about noble gases from the European Cenozoic Rift System are based on either natural gas emissions (Bräuer et al., 2013, 2017; Moreira et al., 2018) or fluid inclusions in crystals from mantellic xenoliths (Buikin et al., 2005; Gautheron et al., 2005; Rizzo et al., 2018, 2021). Natural gas emissions may be affected by atmospheric-crustal contamination during the ascent of magmatic fluids (Barry et al., 2013) that may hide the primitive signature of the gaseous component. For its part, the gas entrapped in fluid inclusions in crystals from mantellic xenoliths could have a different isotopic signature than the one attested by erupted products. To overcome these limitations, we aim at studying the geochemical variability (noble gases, carbon isotopes) of the gas entrapped in fluid inclusions from crystals hosted in tephra erupted by the Pavin's Group of Volcanoes, i.e., the youngest volcanoes of the French Massif Central. We compare the results to the composition of gas found in mantle xenoliths and surface gas emissions. In this study, we couple geochemical markers to barometric estimations from fluid inclusions to decipher the evolution of magmatic gases upon ascent (Boudoire et al., 2018) and discuss the origin of the gas released in the area. To achieve these objectives, we use an innovative approach based on (1) the quantification of the influence of carbonate precipitation on CO_2 densities in fluid inclusions to retrieve barometric estimates, and (2) the first chemical characterization (for the French Massif Central if not for the European Cenozoic Rift System) of the gas entrapped in fluid inclusions in phenocrysts from lavas.

2. Geological context and sampling strategy

The Cenozoic European Volcanic Province (CEVP) was generated by intraplate alkaline volcanism related to the European Cenozoic Rift System (ECRS) surrounding the Alpine orogen (Merle and Michon, 2001; Lustrino and Wilson, 2007) and extending over about 1,500 km. The CEVP consists of three main areas marked by volcanic activity: the French Massif Central, the Rhenish Massif, and the Bohemian Massif (Ulrych et al., 1999). The youngest volcanic activity in the CEVP formed the Pavin maar-crater in the French Massif Central about 7 ka ago (Fig. 1; Juvigné and Mialler, 2016). However, the CEVP still presents proofs of a residual or renewed magmatic activity. The province is characterized by current degassing in mineral springs, mofettes, and through the soil (Bräuer et al., 2013, 2017; Gal et al., 2018; Moreira et al., 2018). Presently active magmatic processes have been

104 recognized or hypothesized during the last 20 years beneath the Cheb basin, in the Bohemian Massif
105 (Bräuer et al., 2011), and in the Eifel region, in the Rhenish Massif (Hensch et al., 2019; Kreemer et
106 al., 2020) with both local seismicity and ground deformation. In the French Massif Central,
107 petrological investigations have suggested the potential presence of one or more magma reservoirs,
108 still partially molten, beneath the Chaîne des Puys (Martel et al., 2013; France et al., 2016; Boivin et
109 al., 2017). These inferences on the current state of magmatic activity in the CEVP, close to densely
110 populated areas, may raise major concerns about civil protection and risk management.

111 The French Massif Central (FMC) is the largest magmatic province of the CEVP and is
112 characterized by typical intraplate alkaline series (Michon and Merle, 2001). The Cenozoic volcanic
113 activity spread over three main periods due to local extension and mantle upwelling of the ECRS: a
114 pre-rift stage (65-34 Ma), a rifting stage (34-15 Ma), and a post-rift stage marked by major magmatic
115 events. The post-rift stage is subdivided into three phases of volcanism. The first phase (9-6.3 Ma) is
116 marked by eruptive activity in the Cantal (**Fig. 1a**), Aubrac, Velay, and Coirons. The second phase
117 (3.5-0.23 Ma) took place mainly in the Monts-Dore (**Fig. 1a**) and Devès. Finally, the most recent one
118 occurred in the Chaîne des Puys (160-6.7 ka; **Fig. 1a**) and Bas-Vivarais (Nomade et al., 2016). The
119 last known eruptive site in the FMC (the Pavin's Group of Volcanoes; 6,730±170 BP; Juvigné and
120 Miallier, 2016) is located at the southern extremity of an alignment of about 80 monogenetic
121 volcanoes oriented N-S and forming the Chaîne des Puys, at the boundary between the Monts-Dore
122 and the Cézallier (**Fig. 1a**). The Pavin's Group of Volcanoes is composed of 4 monogenetic volcanoes
123 that erupted over a short period of time of about 100-700 years (**Fig. 1b**; Juvigné and Miallier, 2016):
124 Montcineyre, Estivadoux, Montchal, and Pavin (from the oldest to the youngest). Volcanic products
125 from these edifices mark a clear trend of magma differentiation from basanite at Montcineyre (the
126 most primitive lavas erupted in this part of the FMC in the last 200 ka) to benmoreite at Pavin (maar-
127 diatreme volcano now filled by a meromictic lake with dissolved gases in depth; Michard et al., 1994;
128 Jézéquel et al., 2016). Very early fractionation of amphibole was recognized (based on K₂O, Sc, Co,
129 Y, Nb, Ta, and REEs contents) in the magmatic series of the Pavin's Group of Volcanoes that differs
130 from the early fractionation of clinopyroxene identified in magmas from the Chaîne des Puys
131 (Villemant et al., 2016). In addition to the abundance of dissolved gases in the monimolimnion layer
132 of the Pavin lake (Aeschbach-Hertig et al., 1999), the area is also characterized by soil CO₂ gas
133 emissions (Gal and Gadalia, 2011; Gal et al., 2018) and by degassing at the Escarot mofettes (less
134 than 3 km-far). There, the ³He/⁴He signature is the most primordial ever found in the FMC and
135 suggests direct gas migration from magmatic reservoir in the SCLM to the surface with only minor
136 crustal contamination during the ascent (Aeschbach-Hertig et al., 1999; Bräuer et al., 2017; Moreira
137 et al., 2018).

138 In this study, fresh glassy lapilli from Montcineyre and Montchal, and pumices from Pavin
139 (outcrop of the Quarry of Fraux) were sampled (**Fig. 1c, d**). Analyses made on tephra favour the
140 preservation of fluid inclusions in host crystals (Klügel et al., 2020), limit the effect of crystal
141 recycling and the amount of xenocrysts (Boudoire et al., 2021), and cover the whole differentiation
142 trend of the magmatic series of the Pavin's Group of Volcanoes (Villemant et al., 2016). In addition,
143 two mantle enclaves from the Puy Gonnard, a part of Puy Beaunit volcano, at the northernmost end
144 of the Chaîne des Puys (**Fig. 1a**), were sampled to allow the comparison between results obtained
145 from fluid inclusions in tephra phenocrysts and mantellic crystals. Puy Beaunit (43,900±5,100 BP) is
146 well known for its exceptional mantle enclave abundance and diversity (Brousse and Rudel, 1964;
147 Féménias et al., 2001, 2004). Based on textural and mineral abundance analysis of thin sections (**Fig.**
148 **2**), these mantle enclaves correspond to a coarse to transitional harzburgite (**Fig. 2a, b**) and a
149 granuloblastic lherzolite (**Fig. 2c, d**) following the nomenclature of mantle enclaves at Puy Beaunit
150 defined by Féménias et al. (2004). The geochemical signatures of Montcineyre basanite and Puy
151 Beaunit melt inclusions (Jannot et al., 2005) are close enough to assume a common mantle source
152 beneath both areas (Villemant et al., 2016). Dissolved gases were also sampled at 70 and 90 m-depth
153 in the Pavin lake together with gas emissions from the Escarot mofettes to compare the chemistry of
154 the gas phase entrapped in fluid inclusions with that of surface gas emissions.

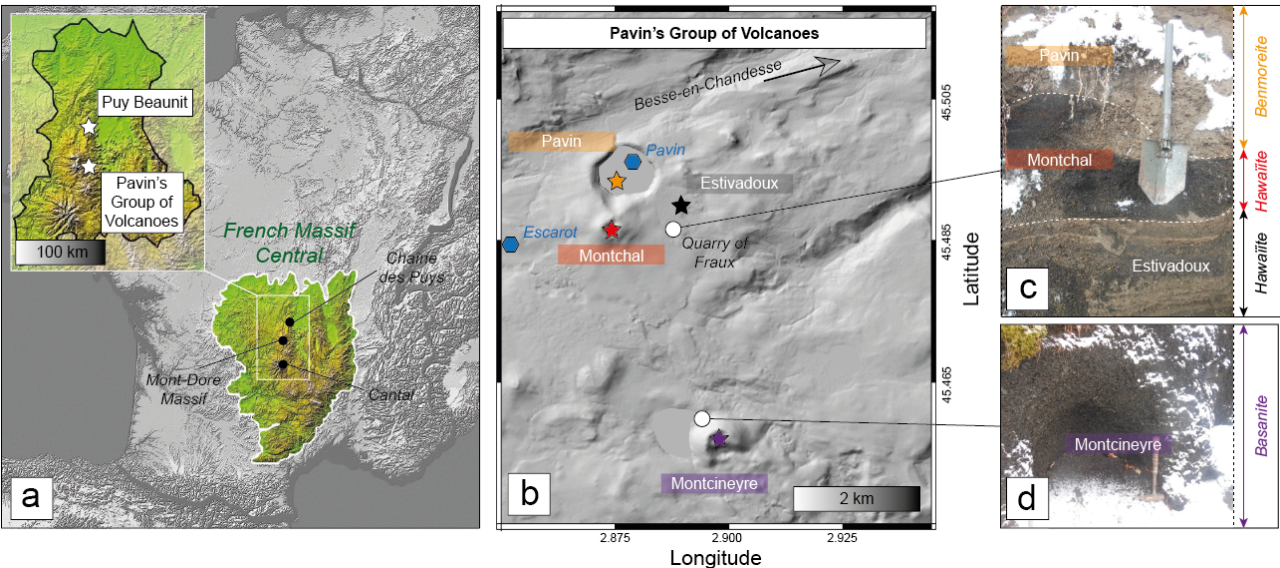


Fig. 1. (a) Location map of the French Massif Central (France) with the two main sampled sites: Puy Beaunit (mantle enclaves) and (b) the Pavin's Group of Volcanoes (lapilli, pumices, dissolved gases in Pavin lake, Escarot mofettes) in the vicinity of the village of Besse-en-Chandesse. (c, d) Photographs of the outcrops where lapilli were sampled.

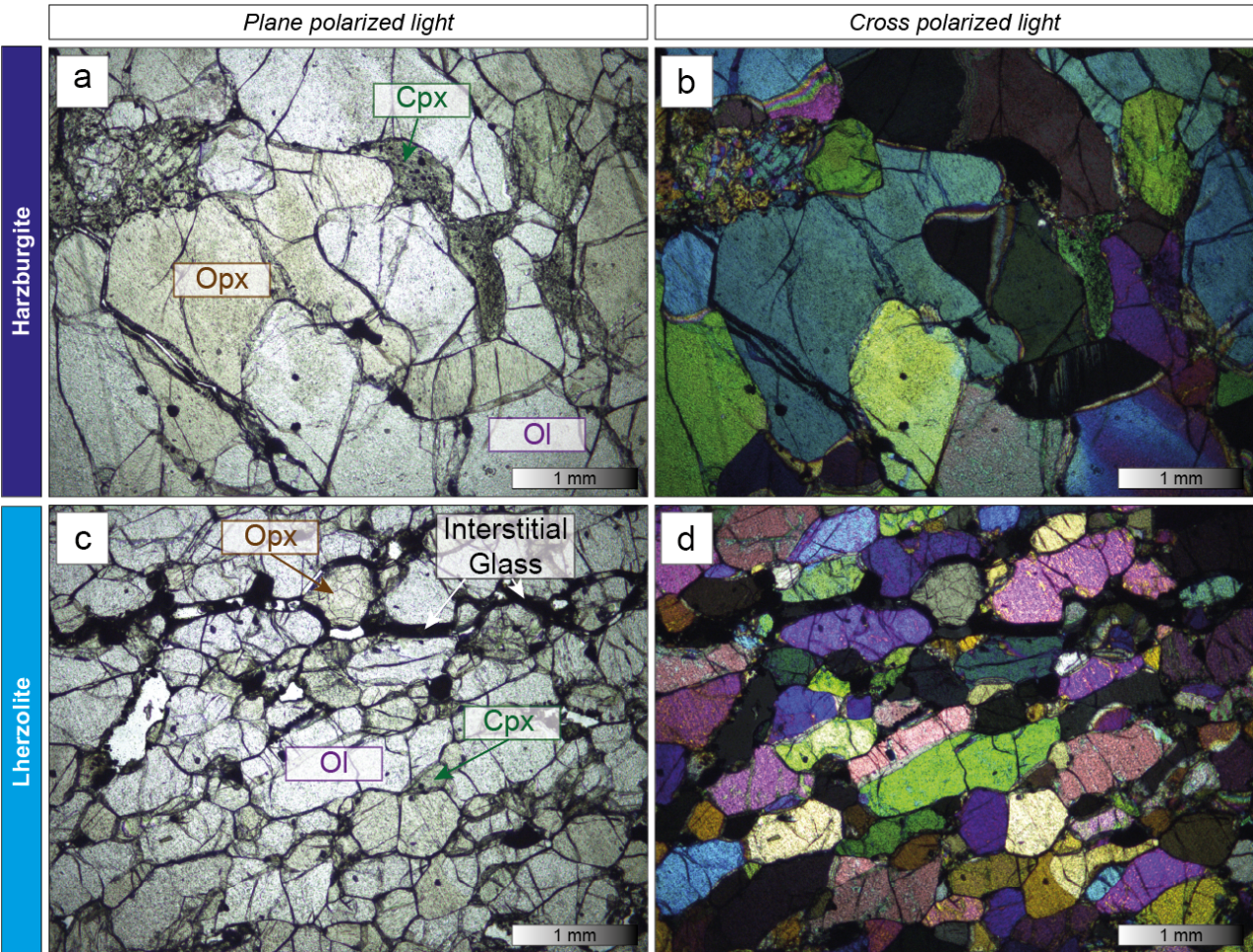


Fig. 2. Transmitted light photomicrographs (in plane and cross polarized light) of the thin sections of two mantle enclaves sampled at Puy Beaunit: (a, b) harzburgite and (c, d) lherzolite (nomenclature of ultramafic rocks from Streckeisen, 1974). Ol, olivine; Cpx, clinopyroxene; Opx, orthopyroxene.

3. Methodology

3.1. Crystal composition

Crystals (olivine, clinopyroxene, orthopyroxene, and amphibole) were hand-picked from crushed and sieved lapilli (Montcineyre, Montchal), pumices (Pavin) and mantle enclaves (Puy Beaunit). Electron microprobe analyses of mineral phases (**Appendix 1**) were performed using a Cameca SXFive at the Laboratoire Magmas et Volcans (Aubière, France) operated with a 15 kV accelerating voltage and a 20 nA current focused beam. Relative errors were 0.5-1.7 % (Si, Mg, Fe, Ca, Al), 16-24 % (Ti, Cr, Mn), and 62-111 % (Ni, K), on average. For olivine, the relative error on CaO was 0.5-15 %. For pyroxene, the relative error on Al₂O₃ was 0.9-3 %.

3.2. Fluid inclusions composition

The composition of the fluid inclusions (**Appendix 2**) was determined at the Laboratoire Magmas et Volcans using an inVia confocal Raman micro-spectrometer manufactured by Renishaw. The micro-spectrometer was equipped with a 532.1 ± 0.3 nm diode laser (200 mW output power), a Peltier-cooled CCD detector of 1040 x 256 pixels, a Rayleigh rejection edge filter, and a Leica DM 2500 M optical microscope with a motorised XYZ stage. Laser power was periodically checked and reduced to 19 mW on the sample surface. A 100x microscope objective, a 20 μ m slit aperture, and a grating of 2400 grooves/mm were used leading to a spectral resolution better than 0.4 cm⁻¹, and spatial resolutions of 1 μ m (horizontal) and 2-3 μ m (vertical) near the surface. Calibration of peak positions was performed based on the 520.5 cm⁻¹ peak of Si and the 1331.5 cm⁻¹ peak of diamond. The spectra were recorded with the WiRE™ 4.2 software in a single window collection (recommended by Lamadrid et al., 2017, for CO₂ densimetry) of 365-1575 cm⁻¹ to cover the vibrational frequencies of mineral phases (host crystals, carbonates, sulphates) and gaseous phases (CO₂-SO₂). Extended spectra were recorded for each family of fluid inclusions (and for each sample) in the wavenumber range 60-4500 cm⁻¹ to investigate the presence of other mineral (sulphides) and fluid phases (H₂O and/or OH molecules). Acquisition time for a single analysis was fixed at 60 s and room temperature was kept at ~20.5 °C.

He (³He, ⁴He), Ne (²⁰Ne), Ar (⁴⁰Ar, ³⁸Ar, ³⁶Ar), C (¹³C/¹²C as $\delta^{13}\text{C}$ versus VPDB reference in per mil) isotopes were measured at the Istituto Nazionale di Geofisica e Vulcanologia (INGV) – Sezione di Palermo. Measurements were performed either in the gas phase entrapped in fluid inclusions hosted in minerals or in surface gas emissions, with small differences in the gas extraction or introduction method as well as in the mass spectrometers used for the analysis. In detail, 0.4-1.2 g of crystals (among olivine, clinopyroxene, orthopyroxene, and amphibole) were hand-picked for noble gases measurements, while 0.5-3.1 g of orthopyroxene for CO₂ extraction and carbon isotopes measurements. Residual glass around the crystals was removed using fluoroboric acid. Then, crystals were cleaned in an ultrasonic bath and loaded in two distinct single-step crushers for the noble gases and CO₂ extraction from fluid inclusions, following the protocols reported in Rizzo et al. (2018, 2021) and Sandoval-Velasquez et al. (2022). After purification and separation of distinct species with cryogenic techniques, He and Ne isotopes were analysed using two distinct split-flight-tube mass spectrometers (Helix SFT-Thermo), and Ar isotopes using a multi-collector mass spectrometer (Argus, GVI). Typical blanks for He, Ne, and Ar were <10⁻¹⁵, <10⁻¹⁶, and <10⁻¹⁴ mol, respectively. The analytical uncertainties (1 σ) for ³He/⁴He are <2.4. The ¹³C/¹²C were measured using a Thermo (Finnigan) Delta Plus XP CF-IRMS connected to a Trace GC gas chromatograph and a Thermo (Finnigan) GC/C III interface. The $\delta^{13}\text{C}$ analytical error is <0.4 ‰ (1 σ). In the case of surface gas emissions samples, an aliquot of gas was introduced in three distinct calibrated pipettes of 0.1 cc each and expanded in three distinct ultra-high-vacuum purification lines dedicated to He, Ne and Ar. After purification procedures, He was introduced in a Helix SFT-GVI, Ne in a Helix MC Plus-Thermo, Ar in a Helix MC-GVI for the respective isotopic measurements, following the purification and analytical protocols reported in Rizzo et al. (2019). Measured ³He/⁴He were corrected for atmospheric

contamination based on their $^4\text{He}/^{20}\text{Ne}$ and the values are expressed as R_c/R_a ($R_a = ^3\text{He}/^4\text{He}$ in air) with:

$$R_c = \frac{(R_m \times (^4\text{He}/^{20}\text{Ne})_m - (^4\text{He}/^{20}\text{Ne})_a)}{((^4\text{He}/^{20}\text{Ne})_m - (^4\text{He}/^{20}\text{Ne})_a)}$$

where R_m and $(^4\text{He}/^{20}\text{Ne})_m$ are the measured values, and $(^4\text{He}/^{20}\text{Ne})_a$ refers to the atmospheric value (0.318; Ozima and Podosek, 2002). ^{40}Ar was also corrected for the atmospheric contamination, as follows:

$$^{40}\text{Ar}^* = ^{40}\text{Ar}_m - (36\text{Ar}_m \times (^{40}\text{Ar}/^{36}\text{Ar})_a)$$

where $^{40}\text{Ar}^*$ is the corrected value, $^{40}\text{Ar}_m$ the measured value, and $(^{40}\text{Ar}/^{36}\text{Ar})_a = 298.56$ (Lee et al., 2006).

3.3. 3D imagery of fluid inclusions

Raman tomography was performed on three fluid inclusions using <5 mW laser power. Acquisitions were collected with a sampling step distance of 0.5-1 μm in the horizontal plane and 1-1.5 μm along the vertical axis, and 10-15 s/point. For each fluid inclusion, 3D mapping produced a single hypermap of ten to fifteen thousand of spectra in the XYZ space. The WiRETM 4.2 software was used to collect, process, and view 3D volume data, allowing spectral information to be analyzed in all dimensions simultaneously. Data processing consisted of several steps. First, narrow random peaks known as cosmic rays were identified and removed from the datasets. Second, the baseline was subtracted from the spectra by fitting the most appropriate polynomial function that passes through anchor points in peak-free spectral regions. After an initial overview of the inclusion volume to recognize the phases present, a representative, well distinct peak, generally corresponding to the strongest vibrational mode, was selected for each phase. A 3D distribution map of the peak intensity was created using the 'signal to baseline' parameter to calculate the area under the selected peak. The volume occupied by each phase was defined by setting a threshold of intensity of the selected peak. To precisely delineate the volume of a phase, horizontal and vertical variations in peak intensity were carefully analyzed, since Raman signal intensity decreases quite rapidly at mineral rims. Volume reconstruction of the inclusion was obtained by merging the 3D maps of all phases into a combined 3D representation on which different phases are identified by different colors. Finally, the recovered volume fraction of each phase was converted to a mass value using the appropriate density. Total CO_2 mass was obtained by adding the mass of fluid CO_2 and that of CO_2 stored in carbonates. Uncertainties in volume reconstruction from Raman tomography are mainly due to the vertical spatial resolution of the technique that can be larger than the size of minerals within the inclusions, resulting in aggregates of very small crystals being represented as large continuous masses. The volumetric reconstruction and associated uncertainties are therefore very sensitive to the intensity threshold defined for data processing. For additional details about the procedure followed for acquisition and processing of 3D maps, and associated uncertainties as well, the reader is referred to Schiavi et al. (2020).

3.4. Barometry based on CO_2 density in fluid inclusions

CO_2 density was calculated from the Fermi dyad split (Δ ; Van den Kerkhof and Olsen, 1990; Frezzotti et al., 2012) between the 1388 and 1285 cm^{-1} peaks (Boudoire et al., 2021). The linearity of the spectrometer was tested by the use of a diamond standard (peak at 1331.5 cm^{-1}). Corrected splitting of the CO_2 Fermi dyad was then determined following the expression (1) of Lamadrid et al. (2017). Using the corrected instead of the measured splitting of the Fermi dyad has a negligible effect on the calculated CO_2 density (<0.01 g/cc). Precautions were taken during the crystal preparation to get homogeneous host crystal radius (around 1 mm) together with limited crystal thickness (between 200

and 400 μm) to reduce the variability of temperatures in fluid inclusions induced by laser heating (Hagiwara et al., 2021a). Based on the equation of Hagiwara et al. (2021b), we estimated a maximum temperature of 42.6 $^{\circ}\text{C}$ for fluid inclusions investigated in this study. For Δ between 102.85 and 105 cm^{-1} , this value of 42.6 $^{\circ}\text{C}$ leads to a maximum uncertainty on CO_2 density of 0.038 g/cc with respect to room temperature by using the equations of Sublett et al. (2020). This part of the uncertainty related to temperature is called hereafter $\varepsilon(\text{temperature})$. If we recognize that the use of Raman spectroscopy at room temperature for the evaluation of CO_2 density in fluid inclusions is not applicable between 0.22 and 0.74 g/cc (coexistence of gas and liquid CO_2), we highlight that, in this study: (i) only 10 fluid inclusions fall in this CO_2 density range (for a total of 70 fluid inclusions) and (ii) laser heating using a 19 mW power on the sample is expected to rise the temperature of fluid inclusions above the critical temperature of CO_2 (31 $^{\circ}\text{C}$; Hagiwara et al. 2021a). Consistently, no moving CO_2 vapour bubble was detected in these fluid inclusions immediately after the analysis arguing for the presence of a homogeneous CO_2 phase during the analysis. Three Raman spectra were acquired for each fluid inclusion to test the reproducibility of the analyses. If the CO_2 densities estimated from these three Raman spectra differ by more than 0.05 g/cc, the fluid inclusion was discarded from the dataset. In this way, the cases of two-phase gas-liquid mixture can also be identified. In the absence of calibrated curves for our instrument (Lamadrid et al., 2017), we tested the reliability of the experimental equations of Song et al. (2009), Fall et al. (2011), Wang et al. (2011) and Lamadrid et al. (2017) on a set of 4 pure CO_2 fluid inclusions (0.60-0.92 g/cc of CO_2 determined by microthermometry) used as internal standards. The equation of Song et al. (2009) provided the most reliable results with a deviation, $\varepsilon(\text{analytical})$, not exceeding 0.037 g/cc of CO_2 , and was used in this study. Finally, the total uncertainty, $\varepsilon(\text{TOT})$, on CO_2 density related to the use of the CO_2 densimeter of Song et al. (2009) and to the analysis of fluid inclusions is (Boudoire et al., 2021):

$$\varepsilon(\text{TOT}) = \sqrt{\varepsilon(\text{analytical})^2 + \varepsilon(\text{temperature})^2 + \varepsilon(\text{processing})^2}$$

where $\varepsilon(\text{processing})$ is the uncertainty related to the spectral resolution by peak fitting (<0.014 g/cc; Kobayashi et al., 2012). In this study $\varepsilon(\text{TOT})$ is equal to 0.054 g/cc, which corresponds to a maximum uncertainty of 70 MPa following the procedure described below. Rare sulphates, sulphides, carbonates, and either liquid or vapor water were sometimes detected in a few fluid inclusions. This observation points to the presence of a CO_2 - H_2O initial mixture (Boudoire et al., 2018, 2021). In agreement with previous inferences made on CO_2 - H_2O initial mixture in fluid inclusions analysed in other similar studies (Hansteen and Klügel, 2008; Zanon and Frezzotti, 2013), we consider an upper limit of 10% mol of H_2O in the initial exsolved phase. Such value leads to a maximum increase of density of 0.03 g/cc. Pressure was estimated with the ISOC code (Bakker, 2003) using the equation of state of Duan et al. (1992, 1996) set for CO_2 - H_2O mixture on a large range of pressure and temperature. Based on the composition of the lavas (Villemant et al., 2016) and the MgO -thermometer of Putirka (2008), the temperature was fixed at 1300 $^{\circ}\text{C}$, 1200 $^{\circ}\text{C}$, and 1050 $^{\circ}\text{C}$ for the basanite of Montcineyre, the hawaiiite of Montchal, and the benmoreite of Pavin. Previous estimations made for the benmoreitic magma of Pavin are in the range 950-975 $^{\circ}\text{C}$ (Rondet et al., 2019). Any uncertainty on temperature results only in minor errors on pressure (<50 MPa for a shift of 100 $^{\circ}\text{C}$). Following the results obtained by Féménias et al. (2001) on mantle enclaves at Puy Beaunit, the temperature was fixed at 850 $^{\circ}\text{C}$ and 1000 $^{\circ}\text{C}$ for granuloblastic lherzolite and transitional harzburgite, respectively. Finally, the cumulated uncertainty on pressure estimates from CO_2 densimetry in fluid inclusions does not exceed 90 MPa in this study.

4. Results

4.1. Mineralogy

The compositions of olivine crystals from the lapilli and pumices of the three volcanoes largely overlap (**Fig. 3a**): from $\text{Fo}_{78.9}$ to $\text{Fo}_{85.8}$ at Montcineyre, from $\text{Fo}_{78.9}$ to $\text{Fo}_{84.1}$ at Montchal, and from

Fo_{77.1} to Fo_{85.3} at Pavin. Meanwhile, the average forsterite content of olivine crystals slightly decreases from Montcineyre (Fo_{83.2}) to Montchal (Fo_{81.1}) and Pavin (Fo_{79.1}) products. Noteworthy, part of olivine crystals from Montcineyre show a lower CaO content (0.12-0.19 wt%) than that from Montchal and Pavin (0.18-0.36 wt%) at constant forsterite content (**Fig. 3a**). The Mg-numbers (Mg#) of olivine crystals from lapilli and pumices differ from the Mg# of olivine crystals at equilibrium with the bulk rock: they are lower at Montcineyre and Montchal, and higher at Pavin (**Fig. 3a**). Both normal and reverse zoning is observed in olivine crystals from Montcineyre and Pavin, whereas only normal zoning was identified in the few analysed olivine crystals from Montchal (**Table 1**). The range of composition of olivine crystals from mantle enclaves is narrow (**Fig. 3a**): from Fo_{89.5} to Fo_{90.1} for the lherzolite and from Fo_{90.5} to Fo_{91.0} for the harzburgite. In both enclaves, an increase of the CaO content at constant forsterite content is observed from crystals core to rim.

As in the case of olivine, the compositions of clinopyroxene crystals from the lapilli and pumices of the three volcanoes overlap widely (**Fig. 3b**): the Mg-number ranges from 72.7 to 84.0 at Montcineyre, from 70.5 to 83.5 at Montchal, and from 74.5 to 79.5 at Pavin. The decrease of the Mg-number of clinopyroxene crystals is coupled with a decrease in SiO₂ and CaO contents and with an increase in Al₂O₃, TiO₂, and Na₂O contents, which mirror the behaviour described for clinopyroxene crystals from mantle enclaves. A few clinopyroxene crystals from Montcineyre display the highest Mg-numbers together with an enrichment in Al₂O₃ and TiO₂ contents. In the same way as for olivine crystals, the Mg-numbers of clinopyroxene crystals from lapilli and pumices differ from the Mg# computed for clinopyroxene at equilibrium with the bulk rock: they are lower at Montcineyre and Montchal, and higher at Pavin (**Fig. 3b**). Complex normal and reverse zoning is observed in clinopyroxene crystals from all lapilli and pumices, whatever the eruptive site (**Table 1**). Clinopyroxene crystals are mainly diopside in both mantle enclaves, lapilli, and pumices. In mantle enclaves, the Mg-number of clinopyroxene crystals decreases (as well as SiO₂ and CaO contents) from harzburgite (Mg# = 91.9±0.7) to lherzolite (Mg# = 89.5±0.6) together with an increase in Al₂O₃ and Na₂O contents (**Fig. 3b, Appendix 1**). No compositional zoning is observed from crystal core to rim.

Orthopyroxene crystals were found only in mantle enclaves. The Mg-number decreases (as well as SiO₂ content) from harzburgite (Mg# = 91.3±0.2) to lherzolite (Mg# = 90.0±0.3) together with an increase in Al₂O₃ and CaO contents. A clear reverse zoning is systematically observed in crystals from both harzburgite and lherzolite (**Fig. 3c**). Amphibole crystals in the pumices of Pavin are kaersutite (Leake et al., 1997).

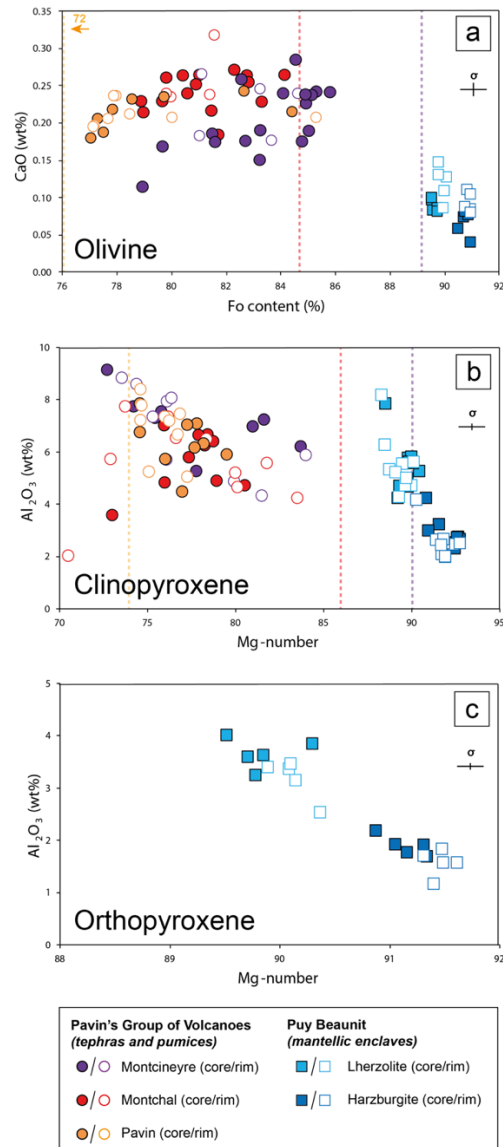


Fig. 3. Composition of (a) olivine, (b) clinopyroxene, and (c) orthopyroxene crystals from mantellic enclaves (Puy Beaunit) and tephtras and pumices (Pavin's Group of Volcanoes). Dashed lines represent the compositions of olivine and clinopyroxene at equilibrium with the bulk rock (Villemant et al., 2016): in purple for Montcineyre (sample P13-8), in red for Montchal (sample P13-4), and in orange for Pavin (sample KBP3b*). For the calculations, the Fe-Mg distribution coefficients between melt and crystals (K_D) were set at 0.30 and 0.27 for olivine and clinopyroxene, respectively (Putirka, 2008).

Δ Mg-number between core and rim	Olivine					Clinopyroxene				
	n	Min	Max	Average	σ	n	Min	Max	Average	σ
Pavin's Group of Volcanoes										
Montcineyre	4	-3.6	0.4	-1.1	1.9	8	-2.4	7.6	0.8	3.5
Montchal	4	0.3	3.3	1.4	1.3	10	-7.0	6.8	0.1	4.8
Pavin	8	-0.9	4.2	0.4	1.6	9	-1.3	3.0	1.2	1.4
Puy Beaunit										
Harzburgite	5	-0.5	0.1	-0.1	0.2	10	-0.7	1.1	0.4	0.6
Lherzolite	5	-0.5	0.0	-0.3	0.2	10	-0.5	1.0	0.4	0.4

Table 1. Difference between the Mg-number calculated for the core and the rim of each single crystal of olivine and clinopyroxene from mantle enclaves (Puy Beaunit) and lapilli and pumices (Pavin's Group of Volcanoes). Negative value denotes a reverse zoning whereas positive value highlights a normal zoning. Note that zoning patterns of clinopyroxene crystals revealed by Backscattered electrons (BSE) imagery during EPMA analyses appear much more complex than

simple normal or reverse zoning and would deserve a dedicated focus that is not the scope of the present study. ‘n’ denotes the number of crystals where the pair core-rim was analysed.

4.2. Fluid inclusions

For lapilli and pumices of the Pavin’s Group of Volcanoes, fluid inclusions were essentially observed in olivine and clinopyroxene crystals. Five families of fluid inclusions were distinguished (**Table 2**): (*F1*) rare primary negatively-shaped fluid inclusions with a homogeneous trapping (**Fig. 4a**), (*F2*) rare pseudo-secondary rounded fluid inclusions with a homogeneous trapping, (*F3*) trails of secondary rounded fluid inclusions with a homogeneous trapping (**Fig. 4b**), (*F4*) primary rounded fluid inclusions with a heterogeneous trapping characterized by the presence of either a single phase or a mixture of liquid-vapour phases and, (*F5*) trails of secondary rounded fluid inclusions with a heterogeneous trapping (**Fig. 4c**). All fluid inclusions are CO₂-rich. Water vapor (3640 cm⁻¹ Raman peak) or a thin film of liquid water on the wall of fluid inclusions (3250-3550 cm⁻¹ Raman band; Frezzotti et al., 2012) were sometimes detected. Additionally, traces of SO₂ (*F1-F5*), carbonates (mainly (Fe-)magnesite and minor Mg-calcite, *F2-F3-F5*), and sulphides (mainly chalcopyrite-pyrite, *F5*) were sometimes detected by Raman spectroscopy (**Appendix 2**).

For mantle enclaves at Puy Beaunit, fluid inclusions were observed in olivine, clinopyroxene, and orthopyroxene crystals. Four families of fluid inclusions were identified (**Table 2**): (*f1*) trails of secondary negatively-shaped fluid inclusions with a homogeneous trapping (**Fig. 4d**), (*f2*) trails of secondary necking down fluid inclusions (**Fig. 4e**), (*f3*) trails of secondary rounded fluid inclusions with a homogeneous trapping (**Fig. 4f**), and (*f4*) trails of secondary rounded fluid inclusions with a heterogeneous trapping. Independently of the family of fluid inclusions, those in crystals from the harzburgite show traces of SO₂ (*f2-f3-f4*). Few crystals from the lherzolite show traces of sulphate (mainly anhydrite and possibly kieserite, *f3*) and carbonate (dolomite, *f3*). Few crystals from the harzburgite show traces of carbonate (mainly dolomite, *f3*) and sulphate (anhydrite, *f3*). Viewable fluid inclusions are abundant in clinopyroxene or orthopyroxene crystals. For the harzburgite, trails of secondary rounded fluid inclusions present in clinopyroxene or orthopyroxene crystals either (1) take a necking down shape (**Fig. 4e**) or (2) are not viewable anymore in adjacent olivine crystals (**Fig. 4f**).

For lapilli and pumices of the Pavin’s Group of Volcanoes, the CO₂ density (ρ) in fluid inclusions is systematically higher than 0.83 g/cc. The maximum of CO₂ density decreases from Montcineyre ($\rho_{\max} = 1.04$ g/cc) to Pavin ($\rho_{\max} = 0.98$ g/cc) and Montchal ($\rho_{\max} = 0.91$ g/cc). For mantle enclaves at Puy Beaunit, the CO₂ density in fluid inclusions covers a larger range of values (from 0.08 to 1.01 g/cc) without clear distinction between harzburgite ($\rho_{\max} = 0.97$ g/cc) and lherzolite ($\rho_{\max} = 1.01$ g/cc). Leaving aside the very low-density values, this range of CO₂ density is close to that reported by Bilal and Touret (1977) for catazonal xenoliths from the Bournac volcano in the FMC (0.72 – 1.08 g/cc). Differences in CO₂ density (average, maximum) among fluid inclusions are noteworthy between (1) primary and secondary/pseudo-secondary fluid inclusions, (2) families of fluid inclusions in each sample, and (3) hosting mineral phases, such as olivine vs. clinopyroxene (**Table 2, Fig. 5**). This phenomenon was extensively documented in other studies focused on fluid inclusions (Hansteen and Klügel, 2008, for a review). These density differences may be related to the history of fluid inclusion entrapment during crystal growth (Hansteen and Klügel, 2008) and/or distinct re-equilibration effects depending on the crystal lattice (Hildner et al., 2011).

Additionally, the effect of the presence of secondary phases in fluid inclusions on CO₂ density was qualitatively evaluated (**Fig. 5, Appendix 2**). No significative difference is observed between pure CO₂-rich fluid inclusions and those characterized by the presence of sulphates or SO₂ (with a low intensity Raman peak at 1148-1150 cm⁻¹) (**Fig. 5a, b**). It is consistent with previous inferences noting that small amounts of additional components in CO₂-dominated fluid inclusions do not affect the interpretation of the trapping conditions (Van den Kerkhof, 1990; Frezzotti et al., 2012). Conversely, we suspect a potential role of carbonate precipitation in the decrease of the CO₂ density in some fluid inclusions belonging to the same family (**Fig. 5c, d**). For instance, the CO₂ density of

the *F5* family in Montcineyre crystals decreases from 1.00 g/cc in fluid inclusions without carbonates to 0.88-0.91 g/cc in fluid inclusions with carbonates. 3D Raman imaging confirmed the presence of accessory carbonate, sulphide, and/or sulphate in some fluid inclusions, especially in the largest ones (**Fig. 6**). Hematite was detected in a large fluid inclusion (**Fig. 6a**). Within a same trail of secondary fluid inclusions in olivine crystals from Montcineyre, the CO₂ density decreases from 1.00 g/cc (FI3 without secondary phases) to 0.92 g/cc (FI2 with carbonate and sulphide), and to 0.88 g/cc (FI1 with carbonate, sulphide, and hematite). This evolution also mirrors a change in the diameter of the fluid inclusions, from 3.5 to 11.5 μm (**Fig. 6**). The effect of both carbonate precipitation and volume of fluid inclusions on CO₂ density will be discussed in a following section.

Host mineral		Group	Type	Shape	Trapping	n	Fermi dyad split Δ (cm-1)				CO ₂ -H ₂ O mixture density ρ (g/cc)				Other phases
							Min	Max	Average	σ	Min	Max	Average	σ	
Pavin's Group of Volcanoes															
Montcineyre	Olivine	F5	Secondary	Rounded	Homogenous	8	104.69	105.07	104.79	0.13	0.89	1.04	0.94	0.05	SO2 - Carbonate - Sulphide Carbonate SO2
	Olivine	F3	Secondary	Rounded	Heterogenous	5	104.64	104.97	104.85	0.15	0.88	1.00	0.96	0.06	
	Olivine	F1	Primary	Negatively shaped	Homogenous	2	104.99	105.00	104.99	0.00	1.01	1.01	1.01	0.00	
	Clinopyroxene	F3	Primary	Rounded	Homogenous	9	104.53	104.80	104.66	0.11	0.83	0.94	0.88	0.04	
Montchal	Olivine	F2	Pseudo-Secondary	Rounded	Homogenous	1	104.58	104.58	104.58	0.00	0.85	0.85	0.85	0.00	Carbonate -
	Olivine	F4	Primary	Rounded	Heterogenous	1	104.72	104.72	104.72	0.00	0.91	0.91	0.91	0.00	
	Olivine	F3	Secondary	Rounded	Homogenous	3	104.80	104.90	104.85	0.05	0.94	0.98	0.96	0.02	
Puy Beaunit															
Harzburgite	Orthopyroxene	f3	Secondary	Rounded	Homogenous	4	104.21	104.89	104.70	0.33	0.69	0.97	0.90	0.14	SO2 Carbonate - Sulphate SO2 SO2
	Clinopyroxene	f3	Secondary	Rounded	Homogenous	4	102.92	103.03	102.97	0.04	0.10	0.15	0.13	0.02	
	Olivine	f2	Secondary	Necking	Homogenous	8	104.01	104.45	104.36	0.15	0.60	0.80	0.76	0.06	
	Olivine	f4	Secondary	Rounded	Homogenous	4	104.73	104.75	104.74	0.01	0.91	0.92	0.91	0.00	
Lherzollite	Orthopyroxene	f3	Secondary	Rounded	Heterogenous	8	103.48	104.85	103.84	0.61	0.36	0.96	0.52	0.27	Sulphate Sulphate -
	Clinopyroxene	f3	Secondary	Rounded	Homogenous	2	102.86	102.92	102.89	0.04	0.08	0.10	0.09	0.02	
	Clinopyroxene	f1	Secondary	Negatively shaped	Homogenous	11	104.80	104.98	104.90	0.06	0.94	1.01	0.98	0.02	

Table 2. Number of analysed fluid inclusions (n), Fermi dyad split (Δ), CO₂ density (ρ) (by considering the presence of a CO₂-H₂O initial mixture), and secondary phases detected by Raman spectroscopy for each family of fluid inclusions (*F1-F5* for the Pavin's Group of Volcanoes and *f1-f4* for Puy Beaunit; see text for explanation). Max: maximum. Min: minimum. Av: average. The standard deviation (σ) on the average was also calculated.

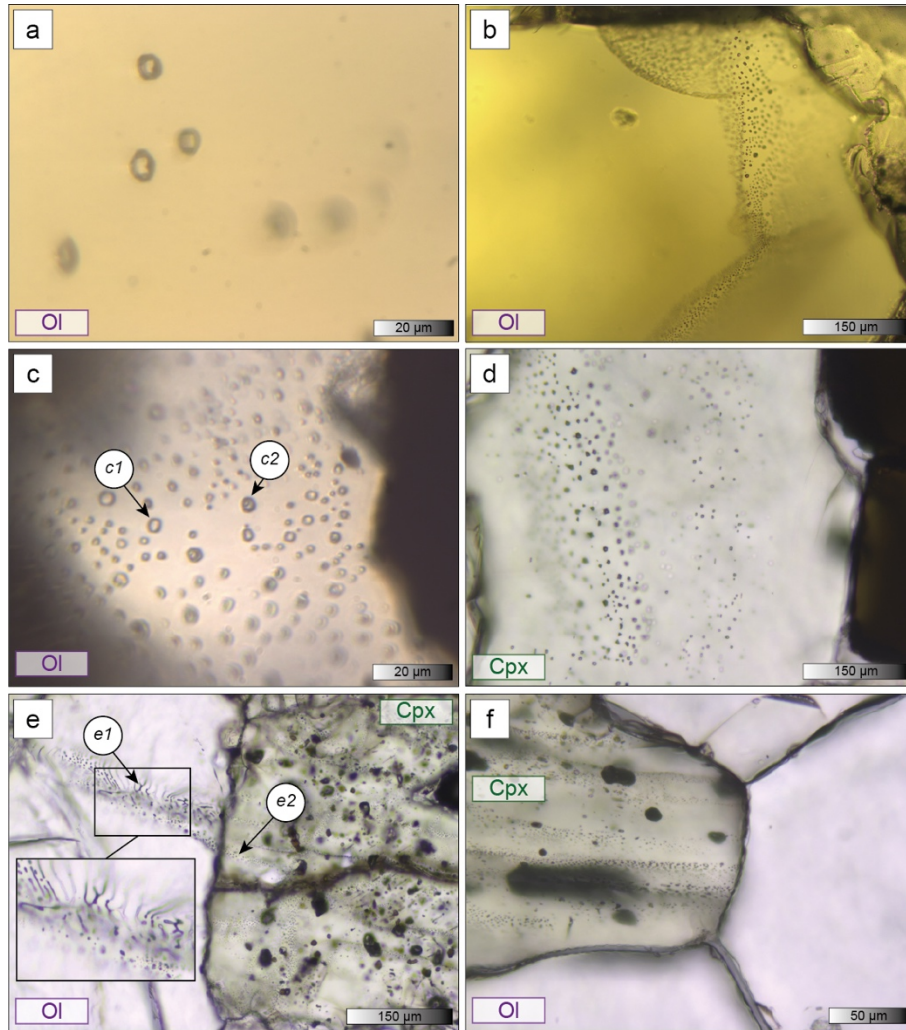


Fig. 4. Transmitted light photomicrographs of the families of fluid inclusions (see text for explanations) in crystals from lapilli and pumices (Pavin's Group of Volcanoes) and mantle enclaves (Puy Beaunit). (a) Primary negatively-shaped fluid inclusions (*FI*) in an olivine crystal from Montcineyre. (b) Secondary rounded fluid inclusions (*F3*) in an olivine crystal from Montcineyre. (c) Secondary rounded fluid inclusions (*F5*) from an olivine crystal from Montcineyre that present a heterogeneous trapping with both single-phase fluid inclusions (*c1*) and a mixture of liquid-vapor phases (*c2*). (d) Secondary negatively-shaped fluid inclusions (*FI*) in a clinopyroxene crystal from the Iherzolite. (e) Continuous trail of secondary fluid inclusions cutting both olivine and clinopyroxene crystals from the harzburgite. Note the inclusions of olivine in the clinopyroxene crystal. Fluid inclusions have a necking down shape in the olivine crystal (*e1*) but are rounded in the clinopyroxene crystal (*e2*). (f) Trail of secondary fluid inclusions in a clinopyroxene crystal from the harzburgite that stops at the contact with the olivine crystal.

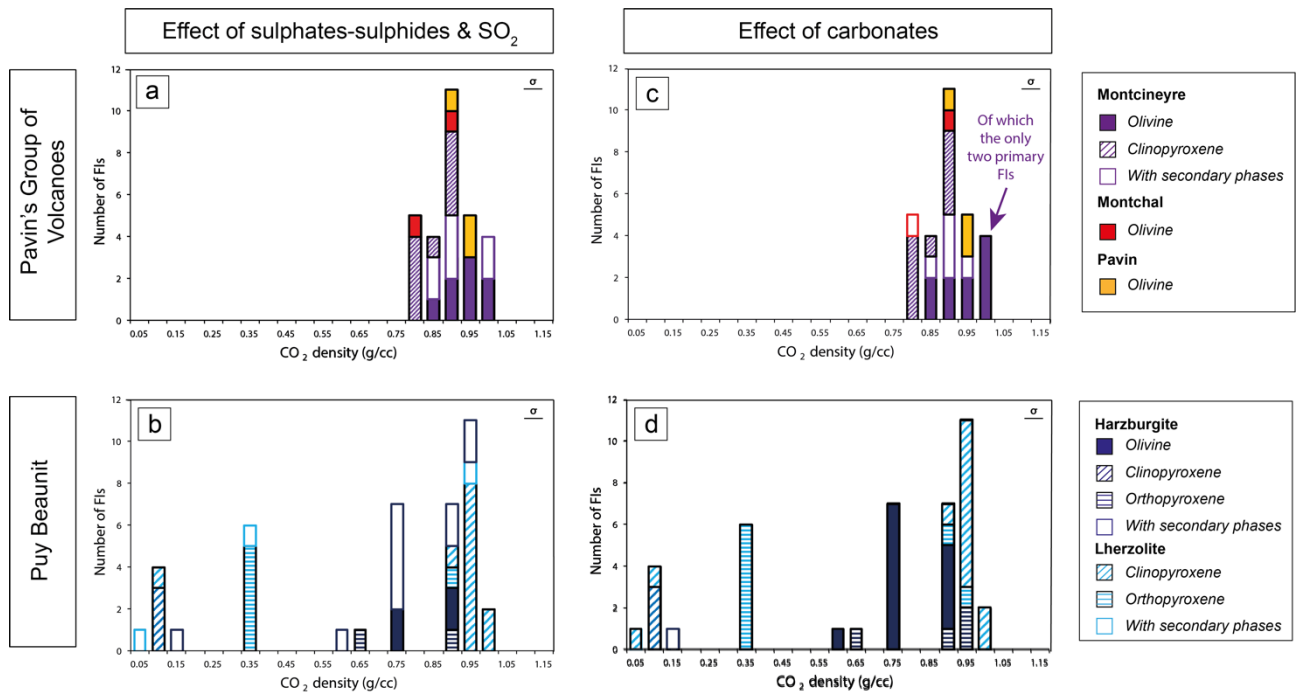


Fig. 5. Distribution of CO₂ density in fluid inclusions from olivine, clinopyroxene, and orthopyroxene from mantle enclaves (Puy Beaunit) and lapilli and pumices (Pavin's Group of Volcanoes). FIs: Fluid Inclusions. "With secondary phases" designs the crystals where either sulphate-sulphide-SO₂ or carbonate were detected in fluid inclusions by Raman spectroscopy. (a) and (b) show the effect of the presence of either sulphate-sulphide or SO₂ in fluid inclusions on the distribution of CO₂ densities. (c) and (d) show the effect of the presence of carbonates in fluid inclusions on the distribution of CO₂ densities.

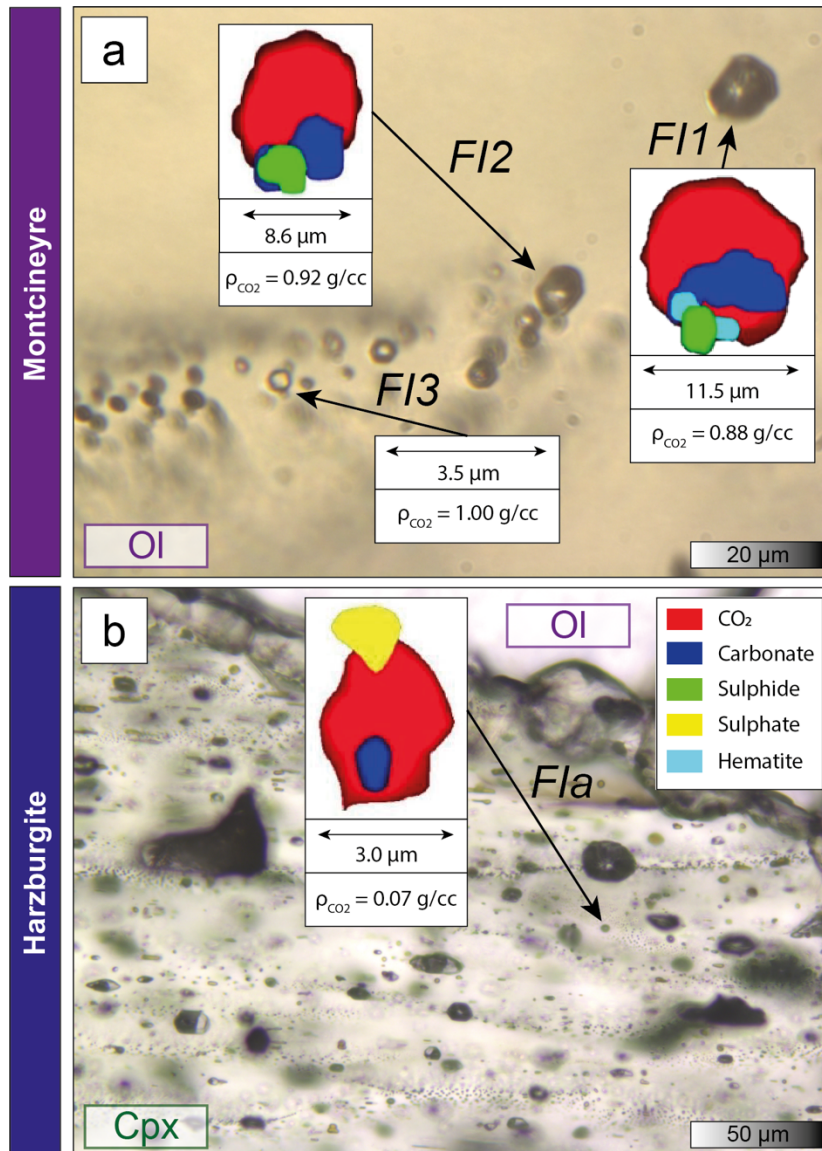


Fig. 6. 2D section of some fluid inclusions extracted from the 3D Raman images. (a) FI1, FI2, FI3 are three single fluid inclusions from a trail of secondary fluid inclusions in an olivine crystal from Montcineyre. (b) Fla is one fluid inclusion in a trail of secondary fluid inclusions cutting clinopyroxene crystal of the harzburgite. The size of the inclusions and the raw CO₂ density (i.e., not calculated by considering the presence of a CO₂-H₂O initial mixture) of the gas phase are reported.

4.3. Noble gases and carbon isotopes of CO₂

Gas content, noble gases, and CO₂ abundances as well as carbon isotopy ($\delta^{13}\text{C}$) of CO₂ obtained by crystal crushing are given in **Table 3**. Helium abundance (^4He) varies from 4.6×10^{-13} mol/g (harzburgite) to 3.5×10^{-12} mol/g (lherzolite) with the highest abundances in orthopyroxene crystals and the lowest ones in olivine crystals. Crystal crushing from the tephra of the Pavin's Group of Volcanoes yields a more restricted range of abundances ($1.2 - 2.0 \times 10^{-12}$ mol/g). $^4\text{He}/^{20}\text{Ne}$ measured in our samples varies from 60 to 5603. Rc/Ra varies from 6.5 to 6.8 Ra for crystals from tephra, with an increase from Pavin to Montchal to Montcineyre products (**Fig. 7a**). Rc/Ra varies from 6.6 to 7.0 Ra for crystals from mantle enclaves, with higher values in orthopyroxene crystals than in olivine ones (**Fig. 7a**). The range of ^4He abundances and Rc/Ra values measured in our study is consistent with previous measurements obtained in mantle enclaves from the CEVP (Buikin et al., 2005; Gautheron et al., 2005; Rizzo et al., 2018, 2021).

The $^{40}\text{Ar}/^{36}\text{Ar}$ varies from 325 to 2735, which is higher than the atmospheric signature ($^{40}\text{Ar}/^{36}\text{Ar} = 298.56$; Lee et al., 2006). $^4\text{He}/^{40}\text{Ar}^*$ ranges from 4.0 to 16.2 for crystals from tephra with an increase from Montcineyre to Montchal to Pavin products (**Fig. 7b**). $^4\text{He}/^{40}\text{Ar}^*$ varies from

0.3 to 1.5 for crystals from mantle enclaves, with the lowest values for the lherzolite (0.3 and 0.7 for orthopyroxene and olivine crystals, respectively). The systematic increase of $^4\text{He}/^{40}\text{Ar}^*$ from orthopyroxene crystals to olivine crystals coupled with a decrease of ^4He abundances (and of Rc/Ra) discards any diffusive fractionation of noble gases between orthopyroxene and olivine crystals (**Fig. 7b**) (Yamamoto et al., 2009; Rizzo et al., 2018, 2021).

The $\text{CO}_2/{}^3\text{He}$ ratio ranges from 1.6×10^8 to 4.0×10^9 for mantle enclaves at Puy Beaunit, with the lowest value measured in olivine crystals and the highest value measured in orthopyroxene crystals from the lherzolite. The range of values for tephra from the Pavin's Group of Volcanoes is narrower ($1.1 - 3.1 \times 10^8$). The analysis of carbon isotopes of CO_2 was possible only by crushing orthopyroxene crystals from both lherzolite and harzburgite due to their higher gas abundance (**Table 3**). $\delta^{13}\text{C}$ of CO_2 varies from -2.9 ‰ for the lherzolite (close to the range of documented values for mantle enclaves within the CEVP) down to -5.8 ‰ for the harzburgite (**Fig. 7c**).

Measurements of dissolved gases in Lake Pavin (at 70 and 90 m-depth) in 2021 yielded Rc/Ra in the range 6.5-6.7, and $\delta^{13}\text{C}$ of CO_2 varying from -2.8 to 0.8 ‰ (**Table 4**). Gas emissions from the Escarot mofettes sampled in 2021 show slightly lower Rc/Ra (= 6.1) and $\delta^{13}\text{C}$ of CO_2 (= -3.4 ‰) than those reported for the Pavin Lake (**Table 4**). The $^4\text{He}/^{40}\text{Ar}^*$ and the $\text{CO}_2/{}^3\text{He}$ are equal to 1.7 and 5.3×10^9 , respectively.

Table 3. Analysis of gas abundance, noble gases, and carbon isotopy ($\delta^{13}\text{C}$) of CO_2 released by crystal crushing.

	Mineral	Absolute Gas Contents										Ratio				Carbon isotopy				
		Gas (mol/g)	⁴ He (mol/g)	³ He (mol/g)	²¹ Ne (mol/g)	³⁶ Ar (mol/g)	³⁸ Ar (mol/g)	⁴⁰ Ar* (mol/g)	CO ₂ (mol/g)	N ₂ (mol/g)	⁴ He/ ²¹ Ne	⁴ He/ ³⁶ Ar*	⁴ He/CO ₂	R/Ra	Rc/Ra	⁴⁰ Ar/ ³⁶ Ar	CO ₂ / ³ He	CO ₂ (mol/g)	δ ¹³ C (‰)	
Pavin's Group of Volcanoes																				
	Montcineyre	Olivine	6.44E-09	2.03E-12	1.93E-17	3.63E-16	1.34E-12	5.17E-16	2.80E-15	5.11E-13	5.89E-09	5.23E-10	5603	3.98	3.45E-04	6.82	6.82	486	3.05E+08	
	Montchal	Olivine	1.61E-09	1.20E-12	1.11E-17	1.82E-15	1.64E-12	9.32E-16	5.14E-15	1.22E-13	1.16E-09	4.14E-10	657	9.82	1.03E-03	6.63	6.63	325	1.05E+08	
	Pavin	Amphibole	3.84E-09	1.16E-12	1.05E-17	3.22E-15	4.63E-13	2.49E-16	1.32E-15	7.19E-14	3.28E-09	5.48E-10	361	16.17	3.54E-04	6.49	6.50	356	3.12E+08	
Puy Beaunit																				
	Harzburgite	Olivine	1.33E-09	4.63E-13	4.33E-18	7.65E-15	3.40E-12	1.88E-15	1.05E-14	3.11E-13	9.49E-10	3.04E-10	60	1.49	4.87E-04	6.71	6.75	331	2.19E+08	
		Orthopyroxene	1.27E-08	1.51E-12	1.47E-17	1.88E-15	2.34E-12	4.37E-16	2.38E-15	1.64E-12	1.17E-08	9.76E-10	802	0.92	1.29E-04	7.00	7.00	1001	7.91E+08	1.06E-08 -5.83
	Lherzolite	Olivine	2.33E-09	7.37E-13	6.81E-18	4.61E-15	2.69E-12	9.68E-16	5.41E-15	1.09E-12	1.06E-09	1.23E-09	160	0.67	6.94E-04	6.62	6.63	507	1.56E+08	
		Orthopyroxene	1.38E-07	3.50E-12	3.34E-17	4.96E-15	1.30E-11	8.79E-16	4.83E-15	1.16E-11	1.35E-07	3.44E-09	705	0.30	2.59E-05	6.84	6.84	2735	4.04E+09	1.03E-07 -2.9

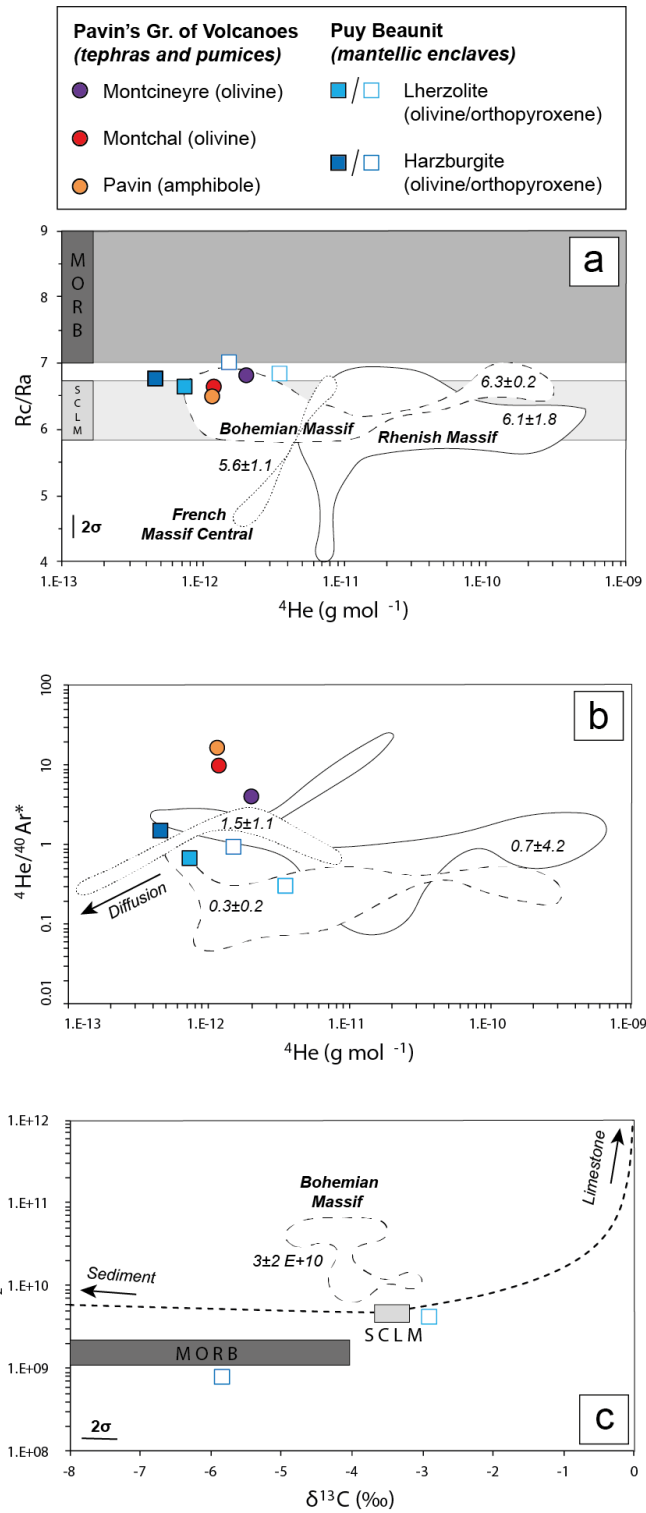


Fig. 7. (a) ^4He abundance vs. R_c/R_a , (b) ^4He abundance vs. $^4\text{He}/^{40}\text{Ar}^*$, and (c) $\delta^{13}\text{C}$ vs. $\text{CO}_2/{}^3\text{He}$ from the gas entrapped in fluid inclusions and released by crystal crushing. The distribution fields of the literature data for the CEVP (French Massif Central, Bohemian Massif, Rhenish Massif) are reported as well as the average value for each field (data sources: Buikin et al. (2005), Gautheron and Moreira (2002), and Rizzo et al. (2018). SCLM, MORB, Limestone and Sediment endmembers from Sano and Marty (1995), Gautheron and Moreira (2002), Bräuer et al. (2016, 2017), and Rizzo et al. (2018).

	$^{40}\text{Ar}/^{36}\text{Ar}$ corr	Error	$^{38}\text{Ar}/^{36}\text{Ar}$ corr	Error	$^4\text{He}/^{20}\text{Ne}$	R/Ra	(R/Ra) _c	Error	$^4\text{He}/^{40}\text{Ar}^*$	$\text{CO}_2/^3\text{He}$	$^4\text{He}/\text{CO}_2$	$\delta^{13}\text{C}$ (‰)
Lac Pavin -70m	296.2	0.1	0.1880	0.0001	10.7	6.55	6.72	0.04		1.31E+09	8.09E-05	0.8
Lac Pavin -90m	296.0	0.1	0.1882	0.0001	4.1	6.02	6.45	0.04		2.07E+09	5.34E-05	-2.8
Escarot	407.2	0.1	0.1862	0.0003	921.0	6.07	6.07	0.03	1.73	5.25E+09	2.24E-05	-3.4

Table 4. Analysis of noble gases and carbon isotopy ($\delta^{13}\text{C}$) of CO_2 in natural gas emissions in the area of study (see Fig. 1).

5. Discussion

5.1. Architecture of the magmatic system beneath the Pavin's Group of Volcanoes

Barometry based on CO_2 density in fluid inclusions is extensively used to decipher the architecture of magmatic systems by pointing out the depth of magma crystallisation and ponding zones during magma ascent (see Hansteen and Klügel (2008) for a complete review). To reach this aim, a careful analysis of the post-entrapment processes that may affect fluid inclusions is required to avoid erroneous interpretation (cf. “Roedder’s rules”; Roedder, 1984). The fluid inclusions FI1-FI2-FI3 described in a trail of secondary fluid inclusions in an olivine crystal from Montcineyre (**Fig. 6a**) are a representative example of a process of CO_2 density decrease due to either post-entrapment volumetric re-equilibration (stretching or decrepitation) or carbonate precipitation (Schiavi et al., 2020; Venugopal et al., 2020). If we assume that the CO_2 density and the volume of FI1-FI2 were identical to those of FI3 at the moment of the entrapment, then the amount of CO_2 in fluid inclusions should remain the same in time, independently of the volumetric change. By considering the volume of FI1-FI2-FI3 and the measured CO_2 density, the amount of CO_2 in fluid inclusions varies by more than an order of magnitude (from 2.2×10^{-11} g of CO_2 in FI3 to $5.9\text{--}6.6 \times 10^{-10}$ g of CO_2 in FI1) (**Table 5**). Accordingly, a scenario of post-entrapment volumetric re-equilibration starting with three inclusions of the same size and density cannot explain the variability of CO_2 density in this trail of secondary fluid inclusions. We recognize that the actual importance of post-entrapment volumetric re-equilibration cannot be quantified precisely because the initial size of the inclusions is not known. However, one can anticipate that this process plays a minor role in explaining the variability of CO_2 density compared to that of carbonate precipitation in our study. Indeed, by using 3D Raman imaging to estimate the amount of CO_2 consumed to form carbonates in FI1 and FI2 (see Methods; Schiavi et al., 2020) we obtain a similar initial CO_2 density for the two inclusions: 1.06 ± 0.09 and 1.12 ± 0.07 g/cc, respectively (instead of a measured CO_2 density of 0.88 and 0.92 g/cc, respectively) (**Table 5**). Considering the total uncertainty, $\varepsilon(\text{TOT})$, on measurements of CO_2 density in fluid inclusions in our study (0.05 g/cc; see Methods), these values overlap with the CO_2 density measured in FI3 (1.0 g/cc) where carbonate was not detected on Raman spectra. A similar calculation was performed in a fluid inclusion (FIa) hosted in a trail of secondary fluid inclusions cutting a clinopyroxene crystal of the harzburgite and where carbonate was detected on Raman spectra (**Fig. 6b**). The CO_2 density increases from 0.14 g/cc (measured) to 0.26 ± 0.09 g/cc (**Table 5**). These calculations show that carbonate formation in fluid inclusions may lead to an underestimation of CO_2 density in fluid inclusions by up to 50 % and thus to unreliable barometric estimates. To limit this effect, in the following parts, we filtered our dataset by considering only fluid inclusions free of solid phases and of small diameter (<4 μm) (**Fig. 8**). The selection of small inclusions is justified because, within the same family of fluid inclusions, secondary solid phases are more abundant and/or CO_2 density is lower in larger fluid inclusions. Such a protocol is in line with previous recommendations made to discard fluid inclusions affected by post-entrapment processes (Wanamaker and Evans, 1989; Frezzotti and Touret, 2014; Boudoire et al., 2018).

Beneath the Chaîne des Puys (close to the area of study; **Fig. 1**), the Moho was imaged at a depth of 24 km, which corresponds to a pressure of about 650 MPa considering an average crustal density of 2750 kg.m^{-3} for the European plate (Spooner et al., 2019). Fixing the temperature at 1300 °C for Montcineyre, 1200 °C for Montchal, and 1050 °C for Pavin (see section 3.4), barometric estimates from the fluid inclusions in crystals from lapilli and pumices of the Pavin's Group of Volcanoes

define two main modes (**Fig. 8a**): (1) at 800-900 MPa and at (2) 600-700 MPa. The first mode is only observed in olivine-hosted fluid inclusions from Montcineyre. A maximum pressure of 903 MPa is recorded in primary fluid inclusions that may represent a deep magma crystallisation zone (of olivine) in the lithospheric mantle. Actually, Montcineyre olivine phenocrysts have the highest average forsterite content (Fo_{83-84}) among the olivine crystals of the Pavin's group of volcanoes. This is consistent with the primitive nature of basanitic lavas erupted at Montcineyre (Villemant et al., 2016), but also shows that advanced differentiation processes already occurred in the lithospheric mantle as the forsterite content in our samples does not exceed $Fo_{85.8}$. The second mode of barometric estimates corresponds to the Moho depth and is defined by most of the secondary fluid inclusions hosted in olivine and clinopyroxene crystals from Montcineyre, Montchal and Pavin. As documented beneath many volcanic provinces (Jennings et al., 2017; Boudoire et al., 2021), the boundary zone between the lithospheric mantle and the crust could be a major interface beneath the area for (1) magma ponding, as indicated by partial or total re-equilibration of some primary fluid inclusions and by the similarity of CO_2 density in distinct families of fluid inclusions (**Table 2**), (2) magma mixing, as suggested by the complex normal and reverse zoning patterns observed in both olivine and clinopyroxene crystals, and by their large range of compositions (**Table 1**), and (3) advanced magma differentiation involving olivine and clinopyroxene fractional crystallization (**Fig. 3**). The barometric estimates obtained in our study from Pavin's pumice (596-663 MPa, i.e., Moho depth) differ from pre-eruptive barometric conditions set by experimental petrology (150-200 MPa, i.e., crustal level; Rondet et al., 2019) (**Fig. 8a**). This discrepancy is presumably due to the fact that our barometric estimations are based on fluid inclusions in olivine crystals. Such olivine crystals are rare in Pavin's pumice, in which plagioclase, amphibole and clinopyroxene are the most abundant crystals, and unusual for differentiated benmoreitic magmas (Rondet et al., 2019). They may be either xenocrysts from older surrounding volcanic rock material carried during the explosive eruption (Villemant et al., 2016) or phenocrysts from a more primitive melt that mixed with the benmoreitic magma at crustal level before the eruption. Further work is required to evaluate these hypotheses.

Considering a temperature of 850 °C for the lherzolite and 1000 °C for the harzburgite (see section 3.4), barometric estimates from the fluid inclusions in crystals from mantle enclaves of Puy Beaunit range from 26 to 636 MPa for the harzburgite and from 96 to 624 MPa for the lherzolite with a main mode around 500-550 MPa (**Fig. 8b**). These pressures are essentially crustal and are far from what one may expect for mantle enclaves. Despite the filtering of the fluid inclusions described above, it is clear that the inclusions have undergone post-entrapment re-equilibration processes such as stretching or decrepitation. Interestingly, we note that helium abundances released by crystal crushing from mantle enclaves are quite similar (if not lower) to those from tephra (**Table 3**). This result contrasts with what we observed, for example, at the Piton de la Fournaise volcano, Réunion Island (Boudoire et al., 2018), where the total gas content released by crystal crushing increases with depth. The extensive post-entrapment re-equilibration observed at Puy Beaunit better supports the idea of a partial decrepitation of fluid inclusions during the ascent of the magma carrying the mantle enclaves. The main mode of barometric estimates around 500-550 MPa corresponds to the deepest pressure mode measured in fluid inclusions in phenocrysts from lavas at Puy Beaunit (**Fig. 8b**; Bilal and Touret, 1977). This good pressure match suggests magma ponding at this depth (Bilal and Touret, 1977), in which the pressures in the fluid inclusions from mantle enclaves have been reset.

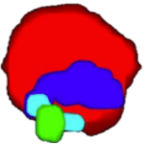
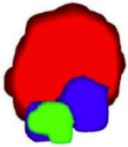
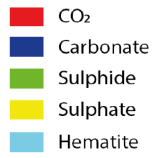
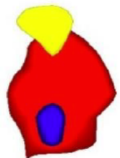
	Montcineyre			Lherzolite
	FI1	FI2	FI3	Fla
				
Measured CO₂ density				
ρ (g/cc)	0.88	0.92	1.00	0.14
Volume				
Spherical Volume (μm^3)	825	332	22	17
Max. Error on Volume (μm^3)	41	15	-	3
Volumetric distribution of the phases				
CO ₂ (%volume)	86	86	100	79
Carbonate (%volume)	10	11	-	6
Sulphide (%volume)	2	3	-	-
Sulphate (%volume)	-	-	-	15
Hematite (%volume)	2	-	-	-
Mass of CO₂ and carbonates				
CO ₂ (g)	(5.94-6.56)E-10	(2.52-2.76)E-10	2.24E-11	(1.43-2.26)E-12
Carbonate (g)	(1.15-1.32)E-10	(5.08-5.80)E-11	-	(1.01-1.87)E-12
Recalculated initial CO₂ density				
ρ (Initial CO ₂) (g/cc)	1.06	1.12	1.00	0.26
σ (g/cc)	0.09	0.07	-	0.09

Table 5. Reconstruction of the initial CO₂ density in some fluid inclusions characterized by the presence of carbonate. ρ is the measured CO₂ density used in this reconstruction (see Methods).

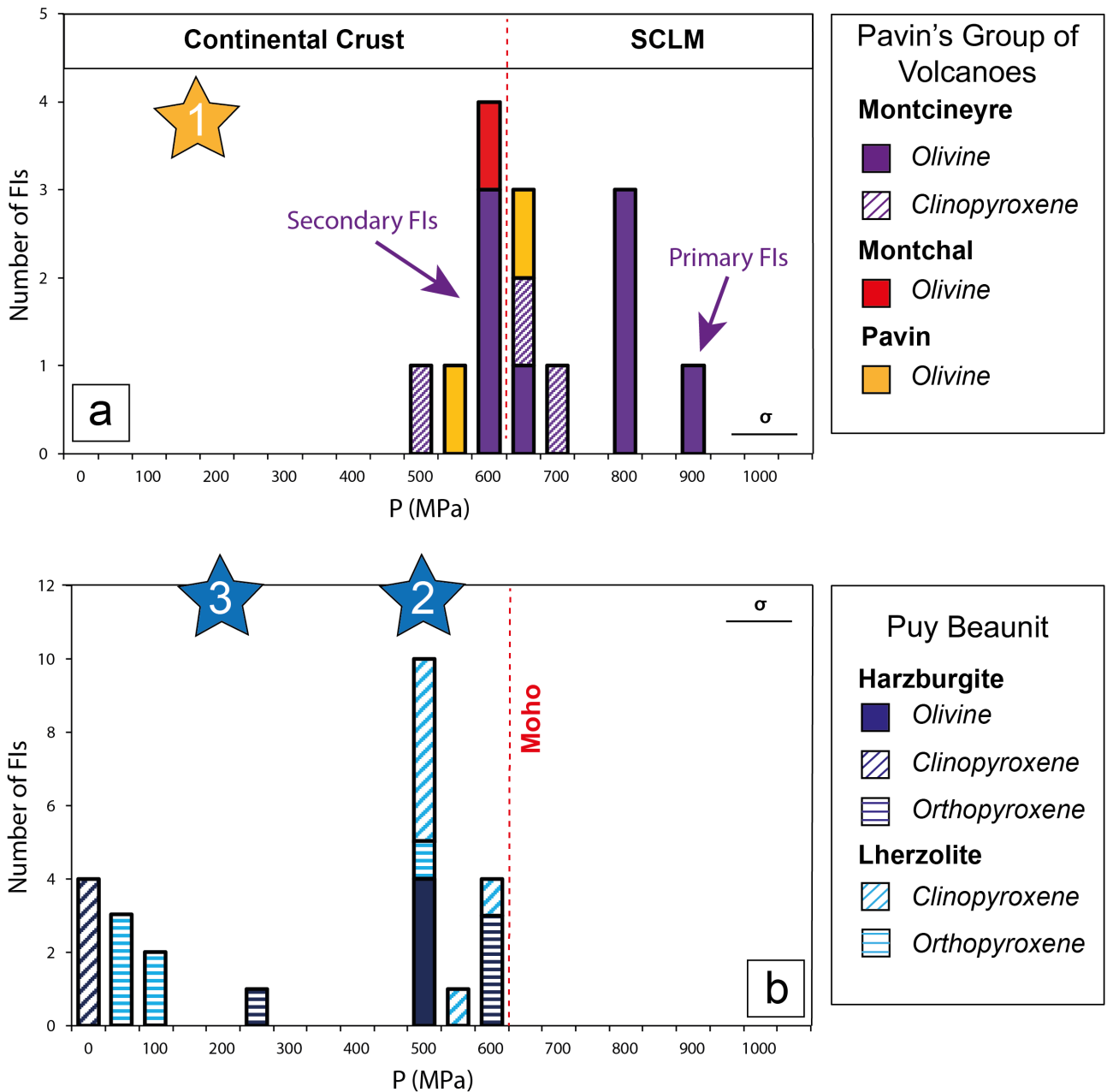


Fig. 8. Distribution of barometric estimates calculated from filtered CO₂ density in fluid inclusions (see Methods) in crystals from (a) tephros of the Pavin's Group of Volcanoes and (b) mantle enclaves at Puy Beaunit. Star no. 1 highlights the pre-eruptive barometric conditions for the Pavin explosive event (Rondet et al., 2019). Stars nos. 2 and 3 are the two barometric modes identified from fluid inclusions in phenocrysts from lavas at Puy Beaunit (Bilal and Touret, 1977).

5.2. Origin and evolution of the magmatic fluids

The Sub-Continental Lithospheric Mantle beneath the FMC was extensively studied by petrological, geochemical, and geophysical means (Lenoir et al., 2000; Féménias et al., 2001, 2004; Babuška et al., 2002; Uenver-Thiele et al., 2014, 2017). Compared to the southern domain, the northern lithospheric domain of the FMC, where our sampling sites are located, is more refractory and oxidized due to several episodes of melt extraction and metasomatism by subduction-related fluids during Variscan times, including local carbonatite metasomatism (Uenver-Thiele et al., 2017). These phenomena are documented in detail in mantle enclaves at Puy Beaunit (Féménias et al., 2004).

In our study, the increase in MgO in olivine, clinopyroxene, and orthopyroxene (**Fig. 3a**) together with the decrease in Al₂O₃ in clinopyroxene and orthopyroxene (**Fig. 3b, c**) from granuloblastic lherzolite to transitional harzburgite are similar to previous observations made beneath the Rhenish Massif, for instance (see Rizzo et al., 2021, for a review). These trends highlight the

transition from a fertile mantle source (Iherzolite) towards a more refractory mantle source (harzburgite) (Arai, 1994; Bonadiman et al., 2011; Upton et al., 2011).

We showed that $^4\text{He}/^{40}\text{Ar}^*$ and $^3\text{He}/^4\text{He}$ (or Rc/Ra) increase while $\text{CO}_2/^3\text{He}$ and $\delta^{13}\text{C}$ decrease from the Iherzolite to the harzburgite (**Fig. 7b**). These trends contrast with the decrease in $^4\text{He}/^{40}\text{Ar}^*$ and $^3\text{He}/^4\text{He}$ classically associated to partial melting (Yamamoto et al., 2009) and rather suggest preferential metasomatic enrichment of the refractory mantle subsequent to partial melting and melt extraction. The slight increase in CaO and MgO in olivine crystal rims as well as the decrease in Al_2O_3 coupled with the increase in MgO in orthopyroxene crystal rims (**Fig. 3a, c**) may testify of this interaction with a metasomatic agent. Higher $^3\text{He}/^4\text{He}$ together with lower $\text{CO}_2/^3\text{He}$ and $\delta^{13}\text{C}$ for harzburgite are consistent with an enrichment due to fluids with MORB-like features (**Fig. 7a, c**). Similar enrichment processes of the SCLM were documented beneath the Bohemian Massif (Matusiak-Malek et al., 2017; Rizzo et al., 2018), the Rhenish Massif (Rizzo et al., 2021), and the FMC (Uenver-Thiele et al., 2017).

In both harzburgite and Iherzolite, we also documented higher $^3\text{He}/^4\text{He}$ ratios and lower $^4\text{He}/^{40}\text{Ar}^*$ ratios in orthopyroxene with respect to olivine (**Fig. 7a, b**). This observation is common in mantle enclaves from the CEVP (Rizzo et al., 2018) and suggests partial recrystallisation of orthopyroxene. Actually, we noted that (1) trails of secondary fluid inclusions preferentially cut orthopyroxene rather than olivine crystals (**Fig. 4e, f**) and (2) gas abundance released by crystal crushing is higher for orthopyroxene. These observations support the idea of preferential recrystallisation and fluid inclusions entrapment in orthopyroxene under the influence of a metasomatic agent.

Noble gases in fluid inclusions in crystals from tephros of the Pavin's Group of Volcanoes exhibit a range of $^3\text{He}/^4\text{He}$ values (6.5-6.8 Ra) similar to the range in mantle enclaves at Puy Beaunit (6.6-7 Ra). These first values obtained from phenocrysts in lavas suggest that the magma erupted at the Pavin's Group of Volcanoes could be directly linked to partial melts from the local SCLM (Rc/Ra from 5.2 to 7.0; Gautheron and Moreira, 2002). The main difference in noble gases between tephros and mantle enclaves concerns $^4\text{He}/^{40}\text{Ar}^*$ (**Fig. 7b**). Higher values for tephros (>4) are not reconcilable with either (1) an effect of various partial melting degrees of the mantle source (Yamamoto et al., 2009), whose $^4\text{He}/^{40}\text{Ar}^*$ values are systematically lower than 1.5, or (2) a process of diffusive fractionation (Trull and Kurz, 1993) that should decrease both $^4\text{He}/^{40}\text{Ar}^*$ and $^3\text{He}/^4\text{He}$.

Conversely, in magmatic rocks, and increase of the $^4\text{He}/^{40}\text{Ar}^*$ can be indicative of a process of magma degassing due to the higher solubility of He in silicate melts with respect to Ar (Burnard, 2004). With the aim of testing this hypothesis, we modelled degassing trends using the equations of Batch Equilibrium Degassing (BED) and of Fractional Equilibrium Degassing (FED) for $^4\text{He}/^{40}\text{Ar}^*$, $^4\text{He}/\text{CO}_2$ and $\delta^{13}\text{C}$ (Jambon et al., 1986; Shaw et al., 2004). The complete description of the equations is detailed in Boudoire et al. (2018). Starting conditions were defined as follows:

- (1) Initial ratios correspond to the values already defined for the SCLM associated to the ECRS (Braüer et al., 2017; Rizzo et al., 2018). $^4\text{He}/^{40}\text{Ar}^*$ was fixed at 1.0. This value is similar to the values measured (i) in fluid inclusions in the orthopyroxene crystals of the harzburgite analysed in this study ($^4\text{He}/^{40}\text{Ar}^* = 0.9$) and (ii) in fluid inclusions in crystals from phlogopite/amphibole-bearing mantle xenoliths along the ECRS (Rizzo et al., 2021). This choice is further supported by the fact that low-silica magmas such as basanites (Montcineyre) cannot be produced by partial melting of dry Iherzolite in the SCLM but rather required the presence of metasomatized lithologies (Pilet, 2015) as suggested for the harzburgite in our study. $^4\text{He}/\text{CO}_2$ was set at 2.5×10^{-5} and $\delta^{13}\text{C}$ at -3.5 ‰. These values are similar to the values proposed by Rizzo et al. (2018). They are also in the range of those defined for the SCLM in Europe ($\delta^{13}\text{C}$ from -3.5 to -2 ‰) by Braüer et al. (2017) and close to the values obtained in fluid inclusions in orthopyroxene crystals from the Iherzolite analysed in this study (**Fig. 7c**).

- (2) Solubilities of He, Ar and CO₂ (S_{He} , S_{Ar} , S_{CO_2}) were estimated for basanitic and benmoreitic melts to cover the magmatic variability of the Pavin's Group of Volcanoes. We used the model of Iacono-Marziano et al. (2010) for He and Ar, and that of Eguchi and Dasgupta (2018) for CO₂ (**Appendix 3**). These models require an estimation of the composition and density of the magma, and of the pressure-temperature conditions. Importantly, S_{He}/S_{Ar} remains quite constant, whereas S_{He}/S_{CO_2} increases during magma ascent (Boudoire et al., 2018). Note that the solubility of CO₂ depends significantly on melt composition, especially for alkaline melts (Iacono-Marziano et al., 2010; Eguchi and Dasgupta, 2018). As a result, the degassing curves show a higher variability of $^4He/CO_2$ (relative to $^4He/^{40}Ar^*$) depending on melt composition.
- (3) The carbon isotope fractionation factor between vapour and melt (Δ) was fixed at 3 ‰ in accordance with the average value of experimental and natural data (Javoy et al., 1978; Aubaud et al., 2005; Paonita et al., 2012).
- (4) The composition of the lava erupted at Montcineyre (sample P13-8; Villemant et al., 2016) and at Pavin (sample KBP3b*; Villemant et al., 2016) was taken as representative of the basanitic and benmoreitic melts, respectively (**Appendix 3**). The density of the melts was calculated from the equation of Lange and Carmichael (1990).
- (5) Temperature was calculated from the composition of the lava by using the equation of Putirka (2008): 1300 °C at Montcineyre and 1050 °C at Pavin. Pressure was fixed at 650 MPa (Moho depth) in accordance with most of the barometric estimates obtained in this study for the products of the Pavin's Group of Volcanoes (**Appendix 3**).

The modelling of magma degassing revealed that the $^4He/^{40}Ar^*$ variability is best explained by a FED process (**Fig. 9a**). The degree of magma degassing increases from Montcineyre (basanite) to Montchal (hawaiite) to Pavin (benmoreite), and thus mirrors the differentiation trend of the Pavin's Group of Volcanoes. We note that even the more primitive melt at Montcineyre, with barometric estimates referring to mantle level, is already strongly degassed ($\approx 80\%$) with respect to primary mantle conditions. This indicates that melts stored in the lithospheric mantle beneath the area have already undergone an advanced degree of degassing and differentiation (in agreement with the absence of olivine crystals with forsterite content exceeding Fo_{85.8}, as discussed above). A similar conclusion was reached in other volcanic systems, such as in oceanic islands at Piton de la Fournaise (Boudoire et al., 2018) or El Hierro (Longpré et al., 2017), and attributed to early magmatic processes occurring in deeper mantle storage zones. Such an advanced degree of degassing is expected to have an important impact on $\delta^{13}C$ values of the vapor phase exsolved from melts of the Pavin's Group of Volcanoes due to preferential partitioning of ^{13}C in gas bubbles (Aubaud et al., 2004). Unfortunately, direct measurements of $\delta^{13}C$ of CO₂ released by crystal crushing was analytically impossible in these samples due to a low gas abundance. By using the same starting conditions than reported above, we can calculate the expected $\delta^{13}C$ of CO₂ in the vapor phase (**Fig. 9b**): from -8.1/-8.3 ‰ at Montcineyre down to -12.7/-13.2 ‰ at Pavin (for a melt composition that spans between basanite and benmoreite). These estimations show that very negative $\delta^{13}C$ values may be reached with a “purely” magmatic contribution without (1) mixing with ^{13}C -depleted compounds (organic matter, C3-C4 plants; Boudoire et al., 2022) or (2) CO₂ condensation process (Mook et al., 1974).

Interestingly, we also observe a slight decrease of $^3He/^4He$ with time in the fluid inclusions of the Pavin's Group of Volcanoes (**Fig. 9c**). This decrease is not reconcilable with degassing processes, as this ratio does not fractionate. More likely, it results from progressive enrichment in 4He due to (1) magma degassing coupled to aging and/or (2) crustal contamination (Kurz et al., 1996; Moreira, 2013). The amount of radiogenic 4He ingrowth from the decay of U and Th over time ($^4He^*$) in magma can be estimated through the equation of Graham et al. (1987):

$$4He^* = 2.8 \times 10^{-8} \times [U] \times \left(4.35 + \frac{Th}{U}\right) \times t$$

722 where ' t ' is the time in Ma, $[U]$ is the uranium concentration (1.3 ppm in sample P13-8 at
723 Montcineyre; Villemant et al., 2016), and Th/U is the thorium-uranium atomic ratio (3.6 for the same
724 sample). Consequently, the increase in $^4\text{He}/^{40}\text{Ar}^*$ coupled with the decrease in $^3\text{He}/^4\text{He}$ could be
725 consistent with a degassing-aging process of the magma that firstly fed the Montcineyre eruption
726 (**Fig. 9c**). However, the aging required to decrease the $^3\text{He}/^4\text{He}$ in the exsolved vapor phase between
727 the eruptions of Montcineyre (oldest) and Pavin (most recent) involves a magma residence of about
728 2,000 yrs. This period of magma residence is higher than the 100-700 yrs period covering the whole
729 eruptive activity of the Pavin's Group of Volcanoes (Juvigné and Miallier, 2016). It suggests that
730 additional ^4He production is required to accelerate the decrease in $^3\text{He}/^4\text{He}$. The enrichment in U-Th
731 in lavas from Montcineyre to Pavin (**Fig. 9c**) through magma differentiation and/or crustal
732 contamination could explain the required excess of ^4He (Villemant et al., 2016).
733

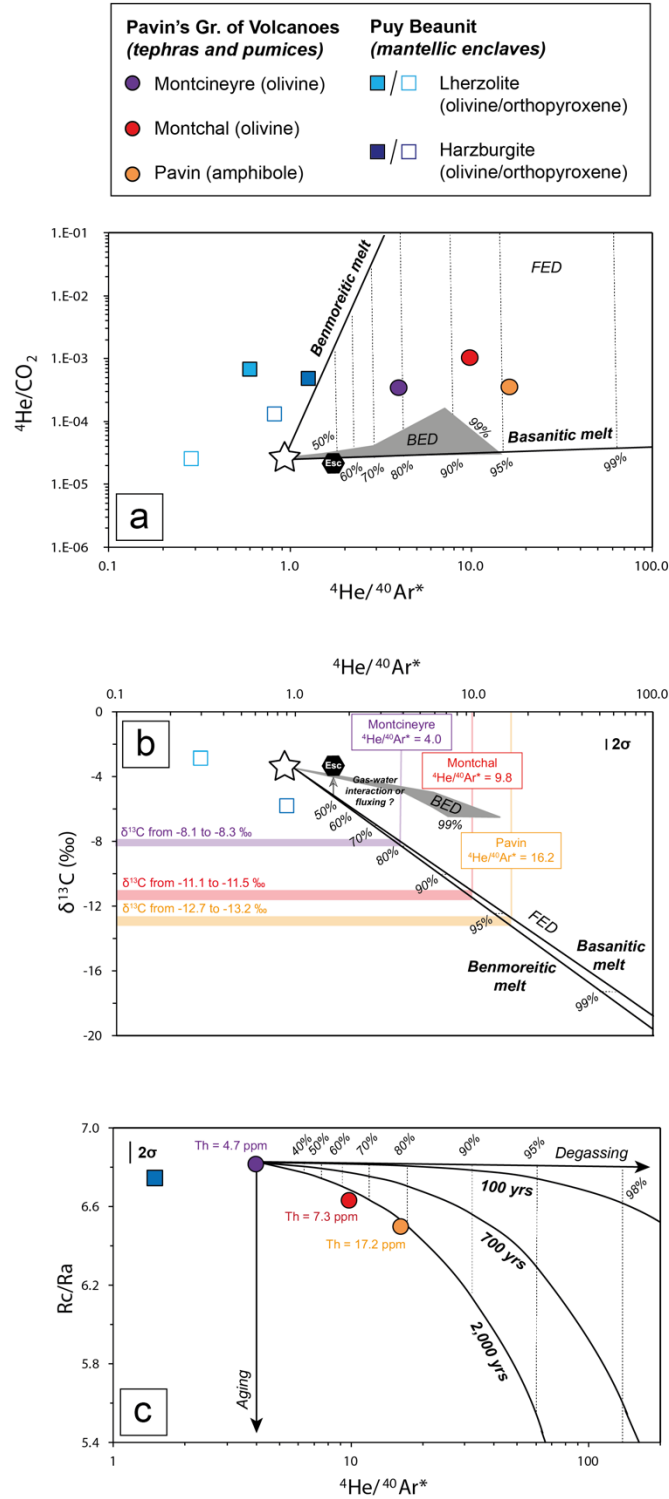


Fig. 9. (a) Modelling of the evolution of $^4\text{He}/^{40}\text{Ar}^*$ and $^4\text{He}/\text{CO}_2$ during degassing. (b) Modelling of the evolution of $\delta^{13}\text{C}$ of CO_2 by degassing. The values of $\delta^{13}\text{C}$ of CO_2 for the vapour phase exsolved from the melts of the Pavin's Group of Volcanoes are estimated by coupling the measured $^4\text{He}/^{40}\text{Ar}^*$ and the theoretical curves of fractional equilibrium degassing for basanitic and benmoreitic melts. (c) Modelling of the aging-degassing processes in the Pavin's Group of Volcanoes: evolution of $^3\text{He}/^4\text{He}$ (Rc/Ra) and $^4\text{He}/^{40}\text{Ar}^*$ in the vapour phase exsolved from the melts. Th is the composition in thorium of the lavas (Villemant et al., 2016). Starting conditions and parameters of modelling are described in the main text. FED: Fractional Equilibrium Degassing. BED: Batch Equilibrium Degassing (grey field for the full field of values considering either a basanitic or a benmoreitic composition). The white star represents the starting conditions in the SCLM (see text for explanations). The black polygon highlights the chemical composition of the gas emissions at the Escarot mofettes.

5.3. Implications for the monitoring of a long-quiet volcanic province

By coupling barometric estimates and the extents of degassing based on $^4\text{He}/^{40}\text{Ar}^*$ (starting from an initial ratio of 1.0 at the source; see previous section) we can build an interpretative scheme of the magma plumbing system beneath Lake Pavin area and of the evolution of the exsolved gas phase (**Fig. 10**). The magma differentiation documented for the Pavin's Group of Volcanoes (Villemant et al., 2016; Rondet et al., 2019) is accompanied by progressive magma degassing together with a decrease of the depth of magma ponding from Montcineyre (basanite, $^4\text{He}/^{40}\text{Ar}^* = 4.0$, Moho depth and deeper) to Montchal (hawaiite, $^4\text{He}/^{40}\text{Ar}^* = 9.8$, Moho depth) to Pavin (benmoreite, $^4\text{He}/^{40}\text{Ar}^* = 16.2$, crustal level).

The model in Figure 10 sheds new light on the origin of current gas emissions in the area. Previous measurements of dissolved gases in Lake Pavin between 1969 and 1996 show an Rc/Ra of 6.5 below the chemocline at 60 m depth (Aeschbach-Hertig et al., 1999; Olive and Boulègue, 2004). Our measurements in 2021 yield a Rc/Ra in the range 6.5-6.7 (**Table 4**) that is consistent with previous analysis. In gas emissions from the Escarot mofettes, a Rc/Ra in the range of 6.0-6.3 and a $\delta^{13}\text{C}$ from -3.8 to -3.6 ‰ were documented in 2011-2015 (Bräuer et al., 2017). The measurements we performed in 2021 (Rc/Ra = 6.1 and $\delta^{13}\text{C} = -3.4$ ‰; **Table 4**) are similar to these values. In addition to the stability of these geochemical markers in time, it is worth noting the high Rc/Ra values in the surface gas emissions, which are the most elevated in the FMC until now (Bräuer et al., 2017). These high Rc/Ra values are close to those documented in the gas entrapped in fluid inclusions from mantle enclaves at Puy Beaunit (Rc/Ra = 6.6-7.0) and from tephra belonging to the Pavin's Group of Volcanoes (Rc/Ra = 6.5-6.8). In addition, $^4\text{He}/^{40}\text{Ar}^*$ was measured at 1.7 in the gas emissions from the Escarot mofettes (**Table 4**). According to our degassing model and interpretative scheme, such value should place the depth of degassing at mantle level (**Fig. 10**). This suggests the absence of residual crustal magma reservoir involved in feeding the surface gas emissions in the Lake Pavin area and rather supports the idea of fluid transport along deep reaching faults from a magma reservoir within the SCLM (Bräuer et al., 2017). However, our interpretative scheme allows us to predict a slight increase in $^3\text{He}/^4\text{He}$ values and in $^4\text{He}/^{40}\text{Ar}^*$ (with respect to current values measured in local gaseous emissions) in the case where a new batch of magma will rise from mantle depth to shallower levels. Considering this scenario, we recommend that an appropriate monitoring strategy for gaseous emissions in the area be put in place.

In our model, $\delta^{13}\text{C}$ of CO_2 should be close to -5.2/-5.4 ‰ in gas emissions from the Escarot mofettes. Such discrepancy with measured value (-3.4 ‰; **Table 4**) is intriguing. A first hypothesis to reconcile these values is to consider a process of partial dissolution of CO_2 in shallow aquifers. Under opportune pH and temperature conditions such a process may trigger the Rayleigh fractionation of CO_2 towards more positive values of $\delta^{13}\text{C}$ (Mook et al., 1974; Hoefs, 1997). It could also partially explain the enrichment in He and CH_4 (Caracausi et al., 2003) with respect to the composition of other local gas emissions (Bräuer et al., 2017). A second hypothesis to explain the relatively high value of $\delta^{13}\text{C}$ of CO_2 measured at the Escarot mofettes is to consider a process of CO_2 fluxing from depth. Indeed, the extensive CO_2 degassing we documented in this study (more than 80 % of the initial CO_2 would be lost for melts of the Pavin's Group of Volcanoes) suggests the presence of a deeper CO_2 vapour phase. This inference is supported by recent results in experimental petrology that show a significative enrichment in volatile elements in primary mantle melts beneath the FMC (Buso et al., 2022). This CO_2 phase, exsolved early and thus characterized by a less negative $\delta^{13}\text{C}$ of CO_2 , may contribute to flux overlying magma reservoirs (Edmonds, 2008) and consequently to modify the pristine signature of the melt-related CO_2 . Carbon dioxide fluxing may also affect the solubility of other gaseous species like H_2O and SO_2 (Spilliaert et al., 2006; Boudoire et al., 2021). This process may provide an explanation to the detection of SO_2 and/or sulphate-sulphide by Raman spectroscopy in some fluid inclusions entrapped at mantle level (**Fig. 5**) whereas SO_2 is expected to strongly degas only at crustal levels (<250 MPa; Boulliung and Wood, 2022). Further work is required to evaluate these hypotheses.

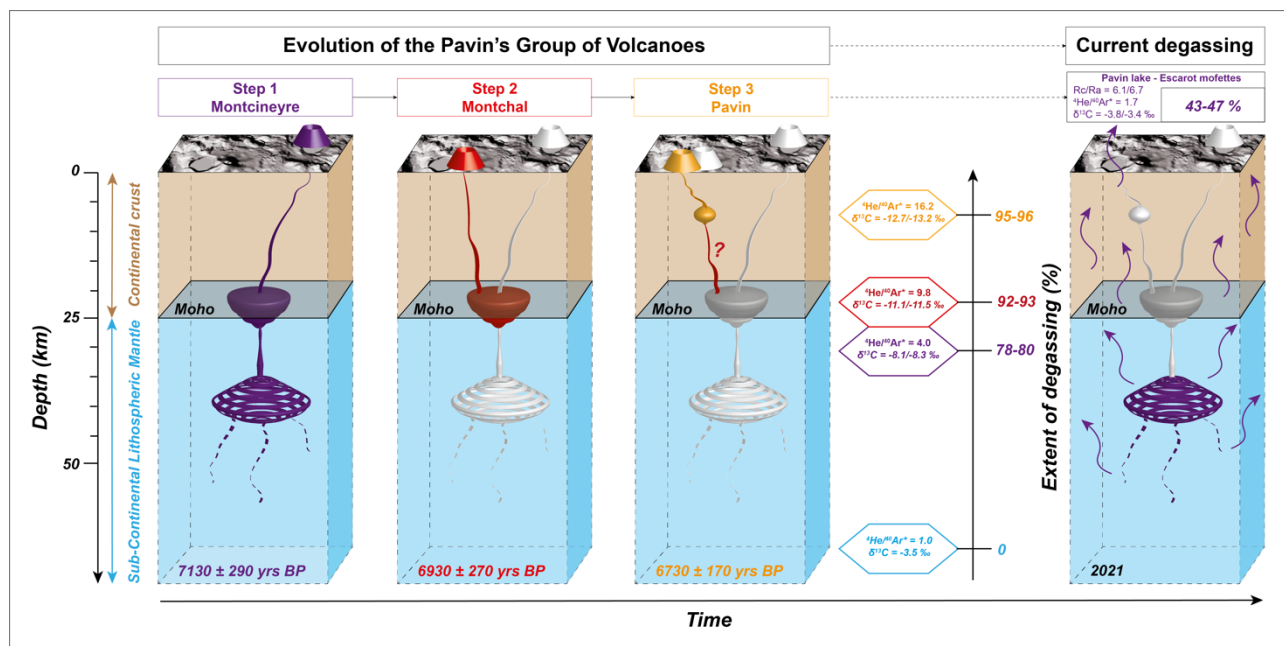


Fig. 10. Interpretative scheme of the evolution in time of the magmatic system and of the composition of the exsolved vapor phase for the Pavin's Group of Volcanoes obtained by coupling (1) barometric estimates, (2) measured $^4\text{He}/^{40}\text{Ar}^*$, (3) estimated $\delta^{13}\text{C}$ of CO_2 from fluid inclusions. A comparison is made with the current status of degassing in the area (composition of dissolved gases in Lake Pavin and of gas emissions from the Escarot mofettes). The question marked in step 3 denotes the hypothesis of a potential pre-eruptive arrival of deep magmatic fluids in the crustal magma reservoir of the Pavin eruption (150-200 MPa; Rondet et al., 2019).

6. Conclusion

We conducted a coupled study of CO_2 densimetry and geochemistry of fluid inclusions from products erupted by the Pavin's Group of Volcanoes, i.e., in the place of the most recent eruptive activity in the French Massif Central. The objectives were to (1) bring new constraints on the architecture of the magmatic system beneath these volcanoes, (2) decipher the evolution of geochemical markers in the gaseous phase exsolved from related magmas, and (3) investigate the origin of current gaseous emissions spread in the area. Our results showed a progressive decrease (in time) of the depth of magma storage (from more than 900 MPa down to 150-200 MPa) in parallel to magma differentiation (from basanites at Montcineyre to benmoreites at Pavin). The geochemical analysis of the noble gases entrapped in fluid inclusions led to two main conclusions. Firstly, $^3\text{He}/^4\text{He}$ ratio (6.5-6.8 Ra) is in the range of ratios measured in fluid inclusions from mantle xenoliths in the Massif Central (5.6 ± 1.1 , on average) in agreement with an origin from the Sub-Continental Lithospheric Mantle (SCLM). Secondly, magma degassing ($^4\text{He}/^{40}\text{Ar}^*$ from 4.0 to 16.2) follows magma differentiation and the progressive rise of the magma ponding zones. Based on these results, we proposed an interpretative scheme of the evolution of the signature of noble gases and carbon isotopes from mantle depth to crustal levels. Gas emissions currently emitted in the area ($R_c/R_a = 6.1-6.7$ and $^4\text{He}/^{40}\text{Ar}^* = 1.7$) points to an origin in the lithospheric mantle according to this model. Meanwhile, an increase in $^3\text{He}/^4\text{He}$ and in $^4\text{He}/^{40}\text{Ar}^*$ in gaseous emissions is expected in the case where a new batch of magma will rise from mantle depth to shallower levels. This inference strongly encourages the establishment of an appropriate monitoring strategy of gaseous emissions in the area.

Acknowledgments

Part of the data were acquired in the frame of the Master thesis of G. Padeloup (Raman analysis of fluid inclusions) at the Laboratoire Magmas et Volcans under the supervision of G. Boudoire, N. Cluzel, F. Schiavi, and A.L. Rizzo. We thank C. Bosq, J-L. Devidal, C. Fonquernie, and E. Voyer at the LMV as well as M. Tantillo, M.G. Misseri, Y. Oliveri, and F. Salerno at the INGV for their priceless support during sample preparation and gas analysis in laboratory. P. Boivin, D. Briot, E.

Médard, and C. Deniel are acknowledged for constructive discussions at the LMV. Data discussed in this study are fully available in Supporting Information. This research is part of the PROVA² initiative held at the OPGC-LMV and has benefited from the Memorandum of Understanding established between the UCA and the INGV. This research was financed by the French Government Laboratory of Excellence initiative n° ANR-10-LABX-0006, the Region Auvergne and the European Regional Development Fund through the project DegazRift. This is Laboratory of Excellence ClerVolc contribution number XXX.

References

- Aeschbach-Hertig, W., Hofer, M., Kipfer, R., Imboden, D. M., & Wieler, R. (1999). Accumulation of mantle gases in a permanently stratified volcanic Lake (Lac Pavin, France). *Geochimica et Cosmochimica Acta*, 63(19-20), 3357-3372.
- Arai, S. (1994). Characterization of spinel peridotites by olivine-spinel compositional relationships: review and interpretation. *Chemical geology*, 113(3-4), 191-204.
- Aubaud, C., Pineau, F., Hékinian, R., & Javoy, M. (2005). Degassing of CO₂ and H₂O in submarine lavas from the Society hotspot. *Earth and Planetary Science Letters*, 235(3-4), 511-527.
- Aubaud, C., Pineau, F., Jambon, A., & Javoy, M. (2004). Kinetic disequilibrium of C, He, Ar and carbon isotopes during degassing of mid-ocean ridge basalts. *Earth and Planetary Science Letters*, 222(2), 391-406.
- Babuška, V., Plomerová, J., Vecsey, L., Granet, M., & Achauer, U. (2002). Seismic anisotropy of the French Massif Central and predisposition of Cenozoic rifting and volcanism by Variscan suture hidden in the mantle lithosphere. *Tectonics*, 21(4), 11-1. <https://doi.org/10.1029/2001TC901035>.
- Bakker, R. J. (2003). Package FLUIDS 1. Computer programs for analysis of fluid inclusion data and for modelling bulk fluid properties. *Chemical Geology*, 194(1-3), 3-23.
- Barry, P. H., Hilton, D. R., Fischer, T. P., De Moor, J. M., Mangasini, F., & Ramirez, C. (2013). Helium and carbon isotope systematics of cold “mazuku” CO₂ vents and hydrothermal gases and fluids from Rungwe Volcanic Province, southern Tanzania. *Chemical Geology*, 339, 141-156.
- Battani, A., Deville, E., Faure, J. L., Jeandel, E., Noirez, S., Tocqué, E., ... & Bauer, A. (2010). Geochemical study of natural CO₂ emissions in the French Massif Central: how to predict origin, processes and evolution of CO₂ leakage. *Oil & Gas Science and Technology–Revue de l’Institut Français du Pétrole*, 65(4), 615-633.
- Bilal, A., & Touret, J. (1977). Les inclusions fluides des phenocristaux des laves basaltiques du Puy Beaunit (Massif Central Français). *Bulletin de Minéralogie*, 100(6), 324-328.
- Boivin, P., Besson, J. C., Briot, D., Camus, G., De Goër de Hervé, A., Gourgaud, A., ... & Livet, M. (2017). *Volcanologie de la Chaîne des Puys. Editions Du Parc Naturel Régional Des Volcans d’Auvergne*, 5th ed. ; IGN : San Francisco, CA, USA.
- Bonadiman, C., Coltorti, M., Beccaluva, L., Griffin, W. L., O’Reilly, S. Y., & Siena, F. (2011). Metasomatism versus host magma infiltration: a case study of Sal mantle xenoliths, Cape Verde Archipelago. *Geol. Soc. Am. Spec. Pap.*, 478, 283-305.
- Boudoire, G., Calabrese, S., Colacicco, A., Sordini, P., Habakaramo Macumu, P., Rafflin, V., ... & Tedesco, D. (2022). Scientific response to the 2021 eruption of Nyiragongo based on the implementation of a participatory monitoring system. *Scientific reports*, 12(1), 1-10.
- Boudoire, G., Di Muro, A., Michon, L., & Metrich, N. (2021). Footprints and conditions of multistep alkali enrichment in basaltic melts at Piton de la Fournaise (La Réunion Island, Indian Ocean). *Bulletin of Volcanology*, 83(12), 1-31.
- Boudoire, G., Rizzo, A. L., Di Muro, A., Grassa, F., & Liuzzo, M. (2018). Extensive CO₂ degassing in the upper mantle beneath oceanic basaltic volcanoes: First insights from Piton de la Fournaise volcano (La Réunion Island). *Geochimica et Cosmochimica Acta*, 235, 376-401.

- Boulliung, J., & Wood, B. J. (2022). SO₂ solubility and degassing behavior in silicate melts. *Geochimica et Cosmochimica Acta*, 336, 150-164.
- Bräuer, K., Geissler, W. H., Kämpf, H., Niedermann, S., & Rman, N. (2016). Helium and carbon isotope signatures of gas exhalations in the westernmost part of the Pannonian Basin (SE Austria/NE Slovenia): Evidence for active lithospheric mantle degassing. *Chemical Geology*, 422, 60-70.
- Bräuer, K., Kämpf, H., Koch, U., & Strauch, G. (2011). Monthly monitoring of gas and isotope compositions in the free gas phase at degassing locations close to the Nový Kostel focal zone in the western Eger Rift Czech Republic. *Chemical Geology*, 290(3-4), 163-176.
- Bräuer, K., Kämpf, H., Niedermann, S., & Strauch, G. (2013). Indications for the existence of different magmatic reservoirs beneath the Eifel area (Germany): A multi-isotope (C, N, He, Ne, Ar) approach. *Chemical Geology*, 356, 193-208.
- Bräuer, K., Kämpf, H., Niedermann, S., & Wetzel, H. U. (2017). Regional distribution pattern of carbon and helium isotopes from different volcanic fields in the French Massif Central: Evidence for active mantle degassing and water transport. *Chemical Geology*, 469, 4-18.
- Brousse, R., & Rudel, A. (1964). Bombes de péridotites, de norites, de charnockites et de granulites dans les scories du Puy Beaunit. *Comptes-rendus de l'Académie des Sciences*, 259(1), 185.
- Brown, S. K., Auken, M. R., & Sparks, R. S. J. (2015). Populations around Holocene volcanoes and development of a Population Exposure Index. *Global volcanic hazards and risk*, 223-232.
- Buikin, A., Tieloff, M., Hopp, J., Althaus, T., Korochantseva, E., Schwarz, W. H., & Altherr, R. (2005). Noble gas isotopes suggest deep mantle plume source of late Cenozoic mafic alkaline volcanism in Europe. *Earth and Planetary Science Letters*, 230(1-2), 143-162.
- Burnard, P. (2004). Diffusive fractionation of noble gases and helium isotopes during mantle melting. *Earth and Planetary Science Letters*, 220(3-4), 287-295.
- Buso, R., Laporte, D., Schiavi, F., Cluzel, N., & Fonquernie, C. (2022). High-pressure homogenization of olivine-hosted CO₂-rich melt inclusions in a piston cylinder: insight into the volatile content of primary mantle melts. *European Journal of Mineralogy Special Volume: Experiments and Mineral Physics at mantle depths. European Journal of Mineralogy*, 34, 325-349. <https://doi.org/10.5194/ejm-34-325-2022>.
- Caracausi, A., Italiano, F., Paonita, A., Rizzo, A., & Nuccio, P. M. (2003). Evidence of deep magma degassing and ascent by geochemistry of peripheral gas emissions at Mount Etna (Italy): Assessment of the magmatic reservoir pressure. *Journal of Geophysical Research: Solid Earth*, 108(B10).
- Chiodini, G., Paonita, A., Aiuppa, A., Costa, A., Caliro, S., De Martino, P., ... & Vandemeulebrouck, J. (2016). Magmas near the critical degassing pressure drive volcanic unrest towards a critical state. *Nature communications*, 7(1), 1-9.
- Duan, Z., Møller, N., & Weare, J. H. (1992). An equation of state for the CH₄-CO₂-H₂O system: I. Pure systems from 0 to 1000 C and 0 to 8000 bar. *Geochimica et Cosmochimica Acta*, 56(7), 2605-2617.
- Duan, Z., Møller, N., & Weare, J. H. (1996). A general equation of state for supercritical fluid mixtures and molecular dynamics simulation of mixture PVTX properties. *Geochimica et Cosmochimica Acta*, 60(7), 1209-1216.
- Edmonds, M. (2008). New geochemical insights into volcanic degassing. *Philosophical Transactions of the Royal Society A: Mathematical, Physical and Engineering Sciences*, 366(1885), 4559-4579.
- Eguchi, J., & Dasgupta, R. (2018). A CO₂ solubility model for silicate melts from fluid saturation to graphite or diamond saturation. *Chemical Geology*, 487, 23-38.
- Fall, A., Tattitch, B., & Bodnar, R. J. (2011). Combined microthermometric and Raman spectroscopic technique to determine the salinity of H₂O-CO₂-NaCl fluid inclusions based on clathrate melting. *Geochimica et Cosmochimica Acta*, 75(4), 951-964.

- Féménias, O., Coussaert, N., Berger, J., Mercier, J. C. C., & Demaiffe, D. (2004). Metasomatism and melting history of a Variscan lithospheric mantle domain: evidence from the Puy Beaunit xenoliths (French Massif Central). *Contributions to Mineralogy and Petrology*, 148(1), 13-28.
- Féménias, O., Mercier, J. C. C., & Demaiffe, D. (2001). Pétrologie des xénolites ultramafiques du puy Beaunit (Massif central français): un gisement atypique du manteau sous-continentale. *Comptes Rendus de l'Académie des Sciences-Series IIA-Earth and Planetary Science*, 332(9), 535-542.
- France, L., Demacon, M., Gurenko, A. A., & Briot, D. (2016). Oxygen isotopes reveal crustal contamination and a large, still partially molten magma chamber in Chaîne des Puys (French Massif Central). *Lithos*, 260, 328-338.
- Frezzotti, M. L., Tecce, F., & Casagli, A. (2012). Raman spectroscopy for fluid inclusion analysis. *Journal of Geochemical Exploration*, 112, 1-20.
- Frezzotti, M. L., & Touret, J. L. (2014). CO₂, carbonate-rich melts, and brines in the mantle. *Geoscience Frontiers*, 5(5), 697-710.
- Gal, F., & Gadalia, A. (2011). Soil gas measurements around the most recent volcanic system of metropolitan France (Lake Pavin, Massif Central). *Comptes Rendus Geoscience*, 343(1), 43-54.
- Gal, F., Leconte, S., & Gadalia, A. (2018). The “Escarot” gas seep, French Massif Central: CO₂ discharge from a quiescent volcanic system—characterization and quantification of gas emissions. *Journal of Volcanology and Geothermal Research*, 353, 68-82.
- Gautheron, C., & Moreira, M. (2002). Helium signature of the subcontinental lithospheric mantle. *Earth and Planetary Science Letters*, 199(1-2), 39-47.
- Gautheron, C., Moreira, M., & Allègre, C. (2005). He, Ne and Ar composition of the European lithospheric mantle. *Chemical Geology*, 217(1-2), 97-112.
- Graham, D. W., Jenkins, W. J., Kurz, M. D., & Batiza, R. (1987). Helium isotope disequilibrium and geochronology of glassy submarine basalts. *Nature*, 326(6111), 384-386.
- Hagiwara, Y., Yoshida, K., Yoneda, A., Torimoto, J., & Yamamoto, J. (2021a). Experimental variable effects on laser heating of inclusions during Raman spectroscopic analysis. *Chemical Geology*, 559, 119928.
- Hagiwara, Y., Kawano, T., Takahata, K., Torimoto, J., & Yamamoto, J. (2021b). Temperature dependence of a Raman CO₂ densimeter from 23° C to 200° C and 7.2 to 248.7 MPa: Evaluation of density underestimation by laser heating. *Journal of Raman Spectroscopy*, 52(10), 1744-1757.
- Hansteen, T. H., & Klügel, A. (2008). Fluid inclusion thermobarometry as a tracer for magmatic processes. *Reviews in Mineralogy and Geochemistry*, 69(1), 143-177.
- Hensch, M., Dahm, T., Ritter, J., Heimann, S., Schmidt, B., Stange, S., & Lehmann, K. (2019). Deep low-frequency earthquakes reveal ongoing magmatic recharge beneath Laacher See Volcano (Eifel, Germany). *Geophysical Journal International*, 216(3), 2025-2036.
- Hildner, E., Klügel, A., & Hauff, F. (2011). Magma storage and ascent during the 1995 eruption of Fogo, Cape Verde Archipelago. *Contributions to Mineralogy and Petrology*, 162(4), 751-772.
- Hoefs, J. (1997). *Stable isotope geochemistry* (Vol. 201). Berlin: Springer.
- Jennings, E. S., Gibson, S. A., MacLennan, J., & Heinonen, J. S. (2017). Deep mixing of mantle melts beneath continental flood basalt provinces: Constraints from olivine-hosted melt inclusions in primitive magmas. *Geochimica et Cosmochimica Acta*, 196, 36-57.
- Iacono-Marziano, G., Paonita, A., Rizzo, A., Scaillet, B., & Gaillard, F. (2010). Noble gas solubilities in silicate melts: new experimental results and a comprehensive model of the effects of liquid composition, temperature, and pressure. *Chemical Geology*, 279(3-4), 145-157.
- Jambon, A., Weber, H., & Braun, O. (1986). Solubility of He, Ne, Ar, Kr and Xe in a basalt melt in the range 1250–1600 C. Geochemical implications. *Geochimica et Cosmochimica Acta*, 50(3), 401-408.

- Jannot S., Schiano P. & Boivin P. (2005). Melt inclusions in scoria and associated mantle xenoliths of Puy Beaunit Volcano, Chaîne des Puys, Massif Central, France. *Contributions to Mineralogy and Petrology*, 149, 600-612.
- Javoy, M., Pineau, F., & Iiyama, I. (1978). Experimental determination of the isotopic fractionation between gaseous CO₂ and carbon dissolved in tholeiitic magma. *Contributions to Mineralogy and Petrology*, 67(1), 35-39.
- Jézéquel, D., Michard, G., Viollier, E., Agrinier, P., Albéric, P., Lopes, F., ... & Bergonzini, L. (2016). Carbon cycle in a meromictic crater lake: Lake Pavin, France. In *Lake Pavin* (pp. 185-203). Springer, Cham.
- Juvigné, E., & Miallier, D. (2016). Distribution, tephrostratigraphy and chronostratigraphy of the widespread eruptive products of Pavin volcano. In *Lake Pavin* (pp. 143-154). Springer, Cham.
- Klügel, A., Day, S., Schmid, M., & Faria, B. (2020). Magma plumbing during the 2014–2015 eruption of Fogo (Cape Verde Islands). *Frontiers in Earth Science*, 8, 157.
- Kobayashi, T., Yamamoto, J., Hirajima, T., Ishibashi, H., Hirano, N., Lai, Y., ... & Arai, S. (2012). Conformity and precision of CO₂ densimetry in CO₂ inclusion
- Kreemer, C., Blewitt, G., & Davis, P. M. (2020). Geodetic evidence for a buoyant mantle plume beneath the Eifel volcanic area, NW Europe. *Geophysical Journal International*, 222(2), 1316-1332.
- Kurz, M. D., Kenna, T. C., Lassiter, J. C., & DePaolo, D. J. (1996). Helium isotopic evolution of Mauna Kea volcano: First results from the 1-km drill core. *Journal of Geophysical Research: Solid Earth*, 101(B5), 11781-11791.
- Lamadrid, H. M., Moore, L. R., Moncada, D., Rimstidt, J. D., Burruss, R. C., & Bodnar, R. J. (2017). Reassessment of the Raman CO₂ densimeter. *Chemical Geology*, 450, 210-222.
- Lange, R. L., & Carmichael, I. S. (1990). Thermodynamic properties of silicate liquids with emphasis on density, thermal expansion and compressibility. *Reviews in Mineralogy and Geochemistry*, 24(1), 25-64.
- Leake, B. E., Woolley, A. R., Arps, C. E., Birch, W. D., Gilbert, M. C., Grice, J. D., ... & Youzhi, G. (1997). Nomenclature of amphiboles; report of the Subcommittee on Amphiboles of the International Mineralogical Association Commission on new minerals and mineral names. *Mineralogical magazine*, 61(405), 295-310.
- Lee, J.-Y., Marti, K., Severinghaus, J. P., Kawamura, K., Yoo, H.-S., Lee, J. B., Kim, J. S. (2006). A Redetermination of the Isotopic Abundances of Atmospheric Ar. *Geochimica et Cosmochimica Acta*, 70, 4507–4512.
- Lenoir, X., Garrido, C. J., Bodinier, J. L., & Dautria, J. M. (2000). Contrasting lithospheric mantle domains beneath the Massif Central (France) revealed by geochemistry of peridotite xenoliths. *Earth and Planetary Science Letters*, 181(3), 359-375.
- Longpré, M. A., Stix, J., Klügel, A., & Shimizu, N. (2017). Mantle to surface degassing of carbon-and sulphur-rich alkaline magma at El Hierro, Canary Islands. *Earth and Planetary Science Letters*, 460, 268-280.
- Lustrino, M., & Wilson, M. (2007). The circum-Mediterranean anorogenic Cenozoic igneous province. *Earth-Science Reviews*, 81(1-2), 1-65.
- Martel, C., Champallier, R., Prouteau, G., Pichavant, M., Arbaret, L., Balcone-Boissard, H., ... & Scaillet, B. (2013). Trachyte phase relations and implication for magma storage conditions in the Chaîne des Puys (French Massif Central). *Journal of Petrology*, 54(6), 1071-1107.
- Matthews, A., Fouillac, C., Hill, R., O'Nions, R. K., & Oxburgh, E. R. (1987). Mantle-derived volatiles in continental crust: the Massif Central of France. *Earth and Planetary Science Letters*, 85(1-3), 117-128.
- Matusiak-Malek, M., Puziewicz, J., Ntaflos, T., Grégoire, M., Kukuła, A., & Wojtulek, P. M. (2017). Origin and evolution of rare amphibole-bearing mantle peridotites from Wilcza Góra (SW Poland), Central Europe. *Lithos*, 286, 302-323.
- Merle, O., & Michon, L. (2001). The formation of the West European Rift; a new model as exemplified by the Massif Central area. *Bulletin de la Société géologique de France*, 172(2), 213-221.

- Michard, G., Viollier, E., Jézéquel, D., & Sarazin, G. (1994). Geochemical study of a crater lake: Pavin Lake, France—Identification, location and quantification of the chemical reactions in the lake. *Chemical Geology*, 115(1-2), 103-115.
- Michon, L., & Merle, O. (2001). The evolution of the Massif Central Rift; spatio-temporal distribution of the volcanism. *Bulletin de la Société géologique de France*, 172(2), 201-211.
- Mook, W. G., Bommerson, J. C., & Staverman, W. H. (1974). Carbon isotope fractionation between dissolved bicarbonate and gaseous carbon dioxide. *Earth and planetary science letters*, 22(2), 169-176.
- Moreira, M. (2013). Noble gas constraints on the origin and evolution of Earth's volatiles. *Geochemical Perspectives*, 2(2), 229-230.
- Moreira, M., Rouchon, V., Muller, E., & Noirez, S. (2018). The xenon isotopic signature of the mantle beneath Massif Central. *Geochem. Perspect. Lett.*, 6, 28-32.
- Nomade, S., Genty, D., Sasco, R., Scao, V., Féruglio, V., Baffier, D., ... & Geneste, J. M. (2016). A 36,000-year-old volcanic eruption depicted in the Chauvet-Pont d'Arc Cave (Ardèche, France)? *PLoS One*, 11(1), e0146621.
- Olive, P., & Boulègue, J. (2004). Étude biogéochimique d'un lac méromictique: le lac Pavin, France/Biogeochemical study of a meromictic lake: Pavin lake, France. *Géomorphologie: relief, processus, environnement*, 10(4), 305-316.
- Oppenheimer, C. (2015). Eruption politics. *Nature Geoscience*, 8(4), 244-245.
- Ozima, M., & Podosek, F. A. (2002). Noble gas geochemistry. Cambridge University Press.
- Paonita, A., Caracausi, A., Iacono-Marziano, G., Martelli, M., & Rizzo, A. (2012). Geochemical evidence for mixing between fluids exsolved at different depths in the magmatic system of Mt Etna (Italy). *Geochimica et Cosmochimica Acta*, 84, 380-394.
- Pilet S. (2015). Generation of low-silica alkaline lavas: Petrological constraints, models, and thermal implications. In Foulger G. R., Lustrino M., and King S. D., eds., *The Interdisciplinary Earth: A Volume in Honor of Don L. Anderson*. Geological Society of America Special Paper 514 and American Geophysical Union Special Publication 71: 281-304.
- Putirka, K. D. (2008). Thermometers and barometers for volcanic systems. *Reviews in mineralogy and geochemistry*, 69(1), 61-120.
- Roedder, E. (1984). Volume 12: fluid inclusions. *Reviews in mineralogy*, 12, 644.
- Rondet, M., Martel, C., & Bourdier, J. L. (2019). The intermediate step in fractionation trends of mildly alkaline volcanic suites: An experimental insight from the Pavin trachyandesite (Massif Central, France). *Comptes Rendus Geoscience*, 351(8), 525-539.
- Rizzo, A. L., Faccini, B., Casetta, F., Faccincani, L., Ntaflos, T., Italiano, F., & Coltorti, M. (2021). Melting and metasomatism in West Eifel and Siebengebirge Sub-Continental Lithospheric Mantle: Evidence from concentrations of volatiles in fluid inclusions and petrology of ultramafic xenoliths. *Chemical Geology*, 581, 120400.
- Rizzo, A. L., Pelorosso, B., Coltorti, M., Ntaflos, T., Bonadiman, C., Matusiak-Malek, M., ... & Bergonzoni, G. (2018). Geochemistry of noble gases and CO₂ in fluid inclusions from lithospheric mantle beneath Wilcza Góra (Lower Silesia, southwest Poland). *Frontiers in Earth Science*, 6, 215.
- Sandoval-Velasquez, A., Rizzo, A. L., Aiuppa, A., Straub, S. M., Gomez-Tuena, A., & Espinasa-Perena, R. (2022). The heterogeneity of the Mexican lithospheric mantle: Clues from noble gas and CO₂ isotopes in fluid inclusions. *Frontiers in Earth Science*.
- Sano, Y., & Marty, B. (1995). Origin of carbon in fumarolic gas from island arcs. *Chemical Geology*, 119(1-4), 265-274.
- Schiavi, F., Bolfan-Casanova, N., Buso, R., Laumonier, M., Laporte, D., Medjoubi, K., Venugopal, S., Gómez-Ulla, A., Cluzel, N., & Hardiagon, M. (2020). Quantifying magmatic volatiles by Raman microtomography of glass inclusion-hosted bubbles. *Geochemical Perspectives Letters*, 16, 17-24.

- Shaw, A. M., Hilton, D. R., Macpherson, C. G., & Sinton, J. M. (2004). The CO₂-He-Ar-H₂O systematics of the Manus back-arc basin: Resolving source composition from degassing and contamination effects. *Geochimica et Cosmochimica Acta*, 68(8), 1837-1855.
- Shoji, S., & Takahashi, T. (2002). Environmental and agricultural significance of volcanic ash soils. *Global Environmental Research-English Edition*, 6(2), 113-135.
- Song, Y., Chou, I. M., Hu, W., Robert, B., & Lu, W. (2009). CO₂ density-Raman shift relation derived from synthetic inclusions in fused silica capillaries and its application. *Acta Geologica Sinica-English Edition*, 83(5), 932-938.
- Spilliaert, N., Allard, P., Métrich, N., & Sobolev, A. V. (2006). Melt inclusion record of the conditions of ascent, degassing, and extrusion of volatile-rich alkali basalt during the powerful 2002 flank eruption of Mount Etna (Italy). *Journal of Geophysical Research: Solid Earth*, 111(B4).
- Spooner, C., Scheck-Wenderoth, M., Götze, H. J., Ebbing, J., Hetényi, G., & AlpArray Working Group. (2019). Density distribution across the Alpine lithosphere constrained by 3-D gravity modelling and relation to seismicity and deformation. *Solid Earth*, 10(6), 2073-2088.
- Streckeisen, A. (1974). Classification and nomenclature of plutonic rocks recommendations of the IUGS subcommission on the systematics of igneous rocks. *Geologische Rundschau*, 63(2), 773-786.
- Sublett Jr, D. M., Sendula, E., Lamadrid, H., Steele-MacInnis, M., Spiekermann, G., Burruss, R. C., & Bodnar, R. J. (2020). Shift in the Raman symmetric stretching band of N₂, CO₂, and CH₄ as a function of temperature, pressure, and density. *Journal of Raman Spectroscopy*, 51(3), 555-568.
- Trull, T. W., & Kurz, M. D. (1993). Experimental measurements of ³He and ⁴He mobility in olivine and clinopyroxene at magmatic temperatures. *Geochimica et cosmochimica acta*, 57(6), 1313-1324.
- Uenver-Thiele, L., Woodland, A. B., Downes, H., & Altherr, R. (2014). Oxidation state of the lithospheric mantle below the Massif Central, France. *Journal of Petrology*, 55(12), 2457-2480.
- Uenver-Thiele, L., Woodland, A. B., Seitz, H. M., Downes, H., & Altherr, R. (2017). Metasomatic processes revealed by trace element and redox signatures of the lithospheric mantle beneath the Massif Central, France. *Journal of Petrology*, 58(3), 395-422.
- Ulrych, J., Pivec, E., Lang, M., Balogh, K., & Kropáček, V. (1999). Cenozoic intraplate volcanic rock series of the Bohemian Massif: a review. *Geolines*, 9, 123-129.
- Upton, B. G. J., Downes, H., Kirstein, L. A., Bonadiman, C., Hill, P. G., & Ntaflos, T. (2011). The lithospheric mantle and lower crust–mantle relationships under Scotland: a xenolithic perspective. *Journal of the Geological Society*, 168(4), 873-886.
- Van den Kerkhof, A. M., & Olsen, S. N. (1990). A natural example of superdense CO₂ inclusions: microthermometry and Raman analysis. *Geochimica et Cosmochimica Acta*, 54(3), 895-901.
- Venugopal, S., Schiavi, F., Moune, S., Bolfan-Casanova, N., Druitt, T., & Williams-Jones, G. (2020). Melt inclusion vapour bubbles: the hidden reservoir for major and volatile elements. *Scientific Reports*, 10(1), 1-14.
- Villemant, B., Caron, B., Thierry, P., & Boivin, P. (2016). Magmatic Evolution of Pavin's Group of Volcanoes: Petrology, Geochemistry and Modeling of Differentiation Processes. A Preliminary Study. In *Lake Pavin* (pp. 129-142). Springer, Cham.
- Wanamaker, B. J., & Evans, B. (1989). Mechanical re-equilibration of fluid inclusions in San Carlos olivine by power-law creep. *Contributions to Mineralogy and Petrology*, 102(1), 102-111.

1192 Wang, X., Chou, I. M., Hu, W., Burruss, R. C., Sun, Q., & Song, Y. (2011). Raman spectroscopic measurements of CO₂
1193 density: Experimental calibration with high-pressure optical cell (HPOC) and fused silica capillary capsule (FSCC) with
1194 application to fluid inclusion observations. *Geochimica et Cosmochimica Acta*, 75(14), 4080-4093.

1195
1196 Yamamoto, J., Nishimura, K., Sugimoto, T., Takemura, K., Takahata, N., & Sano, Y. (2009). Diffusive fractionation of
1197 noble gases in mantle with magma channels: origin of low He/Ar in mantle-derived rocks. *Earth and Planetary Science*
1198 *Letters*, 280(1-4), 167-174.

1199
1200 Zanon, V., & Frezzotti, M. L. (2013). Magma storage and ascent conditions beneath Pico and Faial islands (Azores
1201 archipelago): A study on fluid inclusions. *Geochemistry, Geophysics, Geosystems*, 14(9), 3494-3514.

1202 **Supplementary material**

1203
1204 **Appendix 1.** Composition of the crystals analysed in this study

1205
1206 **Appendix 2.** Composition and CO₂ densimetry of the fluid inclusions

1207
1208 **Appendix 3.** Initial conditions used for the BED and FED modelling.

1209
1210